

An Overview of Condition Monitoring Techniques for Capacitors in DC-Link Applications

Zhaoyang Zhao , Student Member, IEEE, Pooya Davari , Senior Member, IEEE, Weiguo Lu , Member, IEEE,
Huai Wang , Senior Member, IEEE, and Frede Blaabjerg , Fellow, IEEE

Abstract—Capacitors are widely used in dc links of power electronic converters to balance power, suppress voltage ripple, and store short-term energy. Condition monitoring (CM) of dc-link capacitors has great significance in enhancing the reliability of power converter systems. Over the past few years, many efforts have been made to realize CM of dc-link capacitors. This article gives an overview and a comprehensive comparative evaluation of them with emphasis on the application objectives, implementation methods, and monitoring accuracy when being used. First, the design procedure for the CM of capacitors is introduced. Second, the main capacitor parameters estimation principles are summarized. According to these principles, various possible CM methods are derived in a step-by-step manner. On this basis, a comprehensive review and comparison of CM schemes for different types of dc-link applications are provided. Finally, application recommendations and future research trends are presented.

Index Terms—Ceramic capacitors, condition monitoring (CM), dc link, electrolytic capacitors, film capacitors, reliability.

I. INTRODUCTION

C-LINK capacitors are an important part in the majority of electronic converters, which contribute to suppressing dc-link voltage ripple, absorbing harmonics, and balance the instantaneous power difference between the front-end and rear-end of converter systems [1], [2]. In some applications, they are also served to provide sufficient energy for transient and abnormal operations [3], [4]. However, capacitors are sensitive to thermal and electrical stresses and have the main disadvantage of finite lifespan and high degradation failure rate [6]–[8]. As reported in [8], about 30% of the faults in converters are caused by the degradation of capacitors, which makes them to be considered as the

Manuscript received May 27, 2020; revised July 31, 2020; accepted September 8, 2020. Date of publication September 11, 2020; date of current version November 20, 2020. This work was supported by The VELUX Foundations under the VILLUM Investigator Grant REPEPS (Award No. 00016591). Recommended for publication by Associate Editor A. J. Marques Cardoso. (*Corresponding authors:* Huai Wang; Weiguo Lu.)

Zhaoyang Zhao is with the State Key Laboratory of Power Transmission Equipment & System Security and New Technology, Chongqing University, Chongqing 400044, China, and also with the Department of Energy Technology, Aalborg University, 9220 Aalborg, Denmark (e-mail: zhaoyang.z@foxmail.com).

Pooya Davari, Huai Wang, and Frede Blaabjerg are with the Department of Energy Technology, Aalborg University, 9220 Aalborg, Denmark (e-mail: pda@et.aau.dk; hwa@et.aau.dk; fbl@et.aau.dk).

Weiguo Lu is with the State Key Laboratory of Power Transmission Equipment & System Security and New Technology, Chongqing University, Chongqing 400044, China (e-mail: luweiguo@cqu.edu.cn).

Color versions of one or more of the figures in this article are available online at <https://ieeexplore.ieee.org>.

Digital Object Identifier 10.1109/TPEL.2020.3023469

weakest link in power electronic systems [8]. With regard to this, monitoring the degradation state of capacitors and scheduling maintenance before serious degradation or break down occurs have great significance for ensuring the reliable operation of dc-link applications and preventing possible catastrophic failures [9], [10].

In the last two decades, many efforts [11]–[101] have been made to realize the condition monitoring (CM) for capacitors in dc-link applications. Some of them are designed for capacitors dismantled from converters, i.e., offline schemes [11]–[24]. Others are implemented on-site in a real system, i.e., real-online and quasi-online schemes. Here, different types of dc-link applications are considered, such as adjustable speed drive (ASD) systems [25]–[47], photovoltaic (PV) grid-connected inverters [48]–[55], power factor correction (PFC) converters [56]–[61], and dc/dc buck and boost converters [62]–[101]. Moreover, the implementation methods are various. Some schemes monitor the dc-link capacitors using the existing voltage and current information, which can be obtained directly from controllers. Others are based on the signals sampled from additional hardware circuits and sensors. Generally, the research objective and implementation methods of CM are various. It is of great necessity to review these CM techniques for the following purposes.

- 1) Summarize the existing CM techniques and provide a reference for the researchers in this field.
- 2) Benchmark different CM schemes and identify the advantages and limitations of them, in order to provide suggestions for industrial application.
- 3) Analyze the existing challenges and explore future research opportunities.

Recently, some overview papers have been published to review the CM techniques for dc-link capacitors. In [102], Wang *et al.* reviewed the reliability of dc-link capacitors. However, their work mainly focuses on the reliability-oriented design. Only a brief discussion on the CM of dc-link capacitors is given. On this basis, Soliman *et al.* [103] gave a review of the CM of capacitors in power electronic converters. Their work mainly focuses on the classification of the CM techniques. Based on three-category classification methods, the CM techniques are reviewed. Although the above-mentioned review papers give a comparison and analysis for CM techniques of capacitors, there are the following limitations:

- 1) A large amount of latest CM techniques for dc-link capacitors have emerged in recent years, which are not considered in [102] and [103]. Thereby, it is worth to investigate

and discuss on the feasibility of the new state-of-the-art techniques.

- 2) A comprehensive design procedure of CM for capacitors is not given in [102] and [103], which is important for industry application and academic research.
- 3) There is a lack of summarizing of monitoring principles and how to obtain the possible CM methods based on the basic principles.
- 4) No assessment of CM schemes for different types of dc-link applications is provided. For a certain type of converter, such as ASD systems, PV inverters, it is difficult to compare the existing CM schemes.

Therefore, the main goal of this article is to provide a better understanding of both industry and academia on the suitability, feasibility, and implementation of CM schemes by answering the following: 1) What are the possible methods for the CM of capacitors and how to implement them? 2) For a given dc-link application (e.g., ASD systems), what is the difference between the existing CM schemes and how to choose the best one? To answer these questions, this article gives an overview with emphasis on the derivation of CM methods and the discussion of different types of dc-link applications. The main contribution is given as follows.

- 1) A comprehensive design procedure of CM for capacitors is presented.
- 2) Summarizes the main capacitor parameters estimation principles and derives the various possible CM methods in a step-by-step manner.
- 3) Discussion and comparison of the existing CM schemes for main dc-link applications including ASD systems, PV inverters, PFC converters, and dc/dc converters. Based on this, giving suggested solutions for industrial applications.

The rest of this article is organized as follows. Section II presents the design procedure of CM for capacitors. The derivation of CM methods is introduced in Section III. Sections IV to VII are dedicated to the suitability investigation of CM techniques for different types of dc-link applications. Finally, the suggested solutions for industrial applications, future challenges, and opportunities are drawn in Section VIII.

II. DESIGN PROCEDURE FOR CM OF DC-LINK CAPACITORS

A. Capacitors for DC-Link Applications

The typical structure of power electronic systems with dc-link capacitors is shown in Fig. 1. Based on the ripple current limitation of capacitors, a capacitor bank is usually placed at dc link based on series-parallel configuration. Generally, three types of capacitors are used in dc-link applications, which are the Aluminum Electrolytic Capacitors (Al-Caps), Metallized Polypropylene Film Capacitors (MPPF-Caps), and Multi-Layer Ceramic Capacitors (MLC-Caps) [102]. Fig. 2(a) shows a simplified model of the three types of capacitors, where C is the capacitance, R_{ESR} and L_{ESL} represent the equivalent series resistance (ESR) and the equivalent series inductance (ESL), and R_p denotes the insulation resistance. According to the model, the dissipation factor (DF) is defined as $\tan\delta = \omega \cdot R_{\text{ESR}} \cdot C$. The

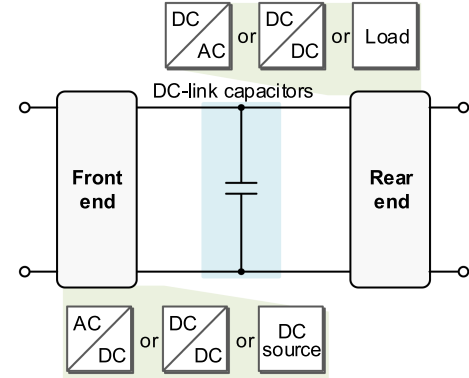


Fig. 1. Typical structure of power electronic systems with dc-link capacitors.

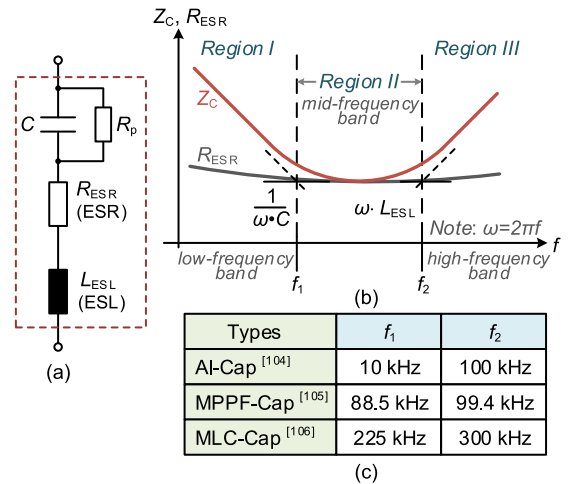
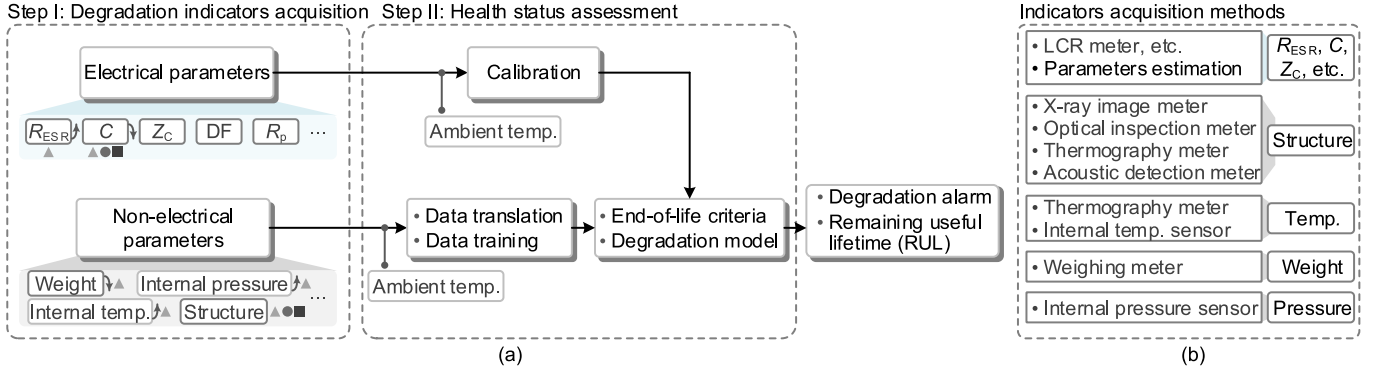


Fig. 2. Equivalent circuit model and impedance characteristics of capacitors. (a) Equivalent circuit model. (b) Impedance characteristics. (c) Typical values of f_1 , f_2 , where the types of Al-Cap, MPPF-Cap, and MLC-Cap are SLPX [104] ($470 \mu\text{F}/450 \text{ V}$), B32778-JX [105] ($480 \mu\text{F}/450 \text{ V}$), and KCM55WC71E107MH13 [106] ($100 \mu\text{F}/25 \text{ V}$), respectively.

impedance Z_C of capacitors is expressed as follows:

$$Z_C = \sqrt{R_{\text{ESR}}^2 + \left(2\pi f \cdot L_{\text{ESL}} - \frac{1}{2\pi f \cdot C}\right)^2}. \quad (1)$$

Using (1), Fig. 2(b) shows the impedance characteristics of capacitors [103]. It is found that the impedance is dominated by the capacitance C in Region I (i.e., low-frequency band, $f \leq f_1$), R_{ESR} in Region II (i.e., mid-frequency band, $f_1 \leq f \leq f_2$), and L_{ESL} in Region III (i.e., high-frequency band, $f \geq f_2$). Taking an Al-Cap, an MPPF-Cap, and an MLC-Cap as examples, Fig. 2(c) gives the typical values of f_1 and f_2 at 25°C [104]–[106], where the types of capacitor are SLPX (Al-Cap, $470 \mu\text{F}/450 \text{ V}$), B32778-JX (MPPF-Cap, $480 \mu\text{F}/450 \text{ V}$), and KCM55WC71E107MH13 (MLC-Cap, $100 \mu\text{F}/25 \text{ V}$), respectively. Notice that C and R_{ESR} are the main degradation indicators of capacitors. Thereby, Region I and Region II (i.e., low-frequency and mid-frequency bands) are considered for CM, which is discussed in the following.



Note: ▲ Suitable indicators for Al-Caps, ● suitable indicators for MPPF-Caps, ■ suitable indicators for MLC-Caps, ↑ indicator increases, ↓ indicator decreases

Fig. 3. CM procedure for dc-link capacitors. (a) CM procedure. (b) Degradation indicators acquisition methods.

B. Design Procedure for CM

With the degradation of dc-link capacitors, a series of physical and chemical changes occur in the inside of capacitors, which will cause electrical parameters (e.g., R_{ESR} , C , Z_C , DF, R_p), and nonelectrical parameters (e.g., weight, structure, internal temperature, internal pressure) to be changed [107]. Generally, these parameters can be chosen as the degradation indicators of capacitors. Based on this, Fig. 3(a) presents a CM procedure for dc-link capacitors. It mainly includes two steps, i.e., degradation indicators acquisition (Step I) and capacitor health status assessment (Step II). For Step I, Fig. 3(b) lists some commonly used parameter acquisition methods. It is found that industrial instruments including weighting meters [108], [109], X-ray image meters [110], optical inspection meter [111], acoustic detection meter [112], thermography meter [113], etc., are widely used to obtain nonelectrical parameters. Moreover, internal temperature sensors [114] and internal pressure sensors [115] are employed to obtain the internal temperature and pressure of capacitors. Due to the electrical parameters and nonelectrical parameters of capacitors are easily influenced by the ambient temperature, it should be considered in Step II.

Considering the electrical characteristics of capacitors, the preferred indicators and their change trends for different types of capacitors are given in Fig. 3. Notice that some electrical parameters, such as Z_C , DF, and R_p can indicate the degradation of capacitors, however, it is difficult to measure them or use them to define the degradation level of capacitors. They are not the best lifetime indicators for CM. Similarly, the suitable nonelectrical indicators are shown in Fig. 3. For Al-Caps, MPPF-Caps, and MLC-Caps, the change of internal structure can be used for CM. However, the changes in weight, internal pressure, and internal temperature are more suitable for Al-Caps.

Generally, electrical parameters can be measured using the LCR meter, impedance analyzer, etc. However, parameter estimation based methods are widely used to estimate the electrical parameters of dc-link capacitors due to the capacitors are not needed to be dismantled from converters in most cases, which will be detailed discussed in Section III.

1) *End-of-Life Criteria:* As mentioned above, R_{ESR} and C are the preferred electrical indicators for the CM

TABLE I
TYPICAL END-OF-LIFE CRITERIA OF CAPACITORS

	Al-Caps	MPPF-Caps	MLC-Caps
End-of-life criteria	$C/C_0 < 80\%$ $R_{ESR}/R_{ESR0} > 2$	$C/C_0 < 95\%$	$C/C_0 < 90\%$

C —capacitance, R_{ESR} —equivalent series resistance, C_0 —initial capacitance, R_{ESR0} —initial equivalent series resistance.

of capacitors. In [102], the typical end-of-life criteria for Al-Caps, MPPF-Caps, and MLC-Caps have been summarized, as shown in Table I. Different from the electrical parameters, the nonelectrical parameters of capacitors are dependent on capacity, materials, rated voltages, and currents. Hence, there are no uniform end-of-life criteria for capacitors when choosing the nonelectrical parameters as the degradation indicators. Generally, two categories of methods are applied to define the end-of-life criteria of capacitors.

One category is to construct the relationship between electrical parameters and nonelectrical parameters, i.e., data translation method. For Al-Caps, capacitor weight, internal pressure, and internal temperature are suitable nonelectrical indicators. Taking weight loss as an example, Fig. 4(a) shows the average weight loss of an Al-Cap (Nichicon PW series, 450 V/68 μ F), Fig. 4(b) gives the relationship between weight loss and R_{ESR} changes [108]. It is found that the weight of capacitors decreases with the degradation of capacitors, the critical weight loss can be defined at a 200% increase in R_{ESR} . However, the weight change is in milligrams, which requires high-accuracy measurement devices.

Another nonelectrical parameter based method is to identify the failure status of capacitors using the structure change of capacitors. Taking the X-ray image based method as an example, Fig. 4(c) shows the X-ray images of a healthy Al-Cap and a failure Al-Cap. However, due to the uncertainty of structure change, it is difficult to construct the relationship between the electrical parameters and structure change. Similarly, the main physical degradation indicator of MLC-Caps and MPPF-Caps is the structure change of capacitors [e.g., internal crack of MLC-Caps, as shown in Fig. 4(d)], which is difficult to construct the relationship between the electrical parameters and nonelectrical

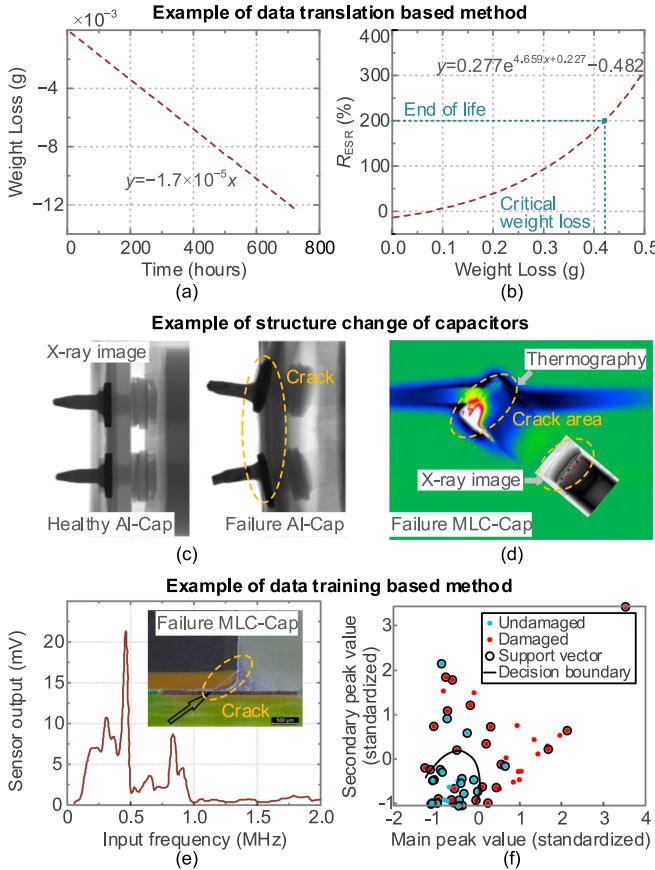


Fig. 4. Example of CM methods based on nonelectrical parameters. (a) Average weight loss of a type of Al-Cap (Nichicon PW series, 450 V/68 μ F) [108]. (b) Weight loss versus R_{ESR} changes of this type of Al-Cap [108]. (c) X-ray images of a healthy Al-Cap and a failure Al-Cap [109]. (d) Thermography and X-ray image of a failure MLC-Cap [113]. (e) Acoustic response of a failure MLC-Cap [112]. (f) SVM classifier fitted into observed MLC-Cap features [112].

parameters. Usually, some data training algorithms are used to distinguish the damaged and undamaged capacitors. In [112], an acoustics detection based method is applied to detect the microcrack of capacitors, as shown in Fig. 4(e). Based on the acoustic response of MLC-Caps, the damaged and undamaged capacitors can be distinguished using a support vector machine (SVM) classifier, as shown in Fig. 4(f).

In summary, nonelectrical parameters based CM schemes generally require high-cost measurement instruments. Moreover, there are no uniform end-of-life criteria, which are not the best schemes for CM.

2) *Degradation Models*: Degradation models are used to calculate the remaining useful lifetime (RUL) of capacitors, which are generally based on electrical parameters. A simple degradation model of Al-Caps is described as [116], [117]

$$\begin{cases} C(t) = C_0 \cdot (1 + A_{\text{Al}} \cdot t) \\ R_{\text{ESR}}(t) = R_{\text{ESR}0} \cdot e^{B_{\text{Al}} \cdot t} \end{cases} \quad (2)$$

where t represents the operation time, C_0 and $R_{\text{ESR}0}$ are the initial capacitance and ESR, respectively. A_{Al} and B_{Al} describe temperature-dependent degradation rates, which can be determined experimentally. For MPPF-Caps, the degradation model

TABLE II
EXPERIMENTAL PARAMETERS OF DEGRADATION MODELS

Cap. types	Experimental parameters	Test condition
Al-Cap [116]	$A_{\text{al}} = -4.899 \times 10^{-6}$, $B_{\text{al}} = 9.547 \times 10^{-5}$	300 kHz @ 54.85–126.85°C
MPPF-Cap [118]	$\lambda_1 = 4.91 \times 10^{-8}$, $\lambda_2 = 0.001$	Rated voltage @ 85 °C
MLC-Cap [119]	k equals to 0 (for COG-type), 2.5 (for X7R-type), 7 (for Y5V-type).	2 times rated voltage @ 125°C

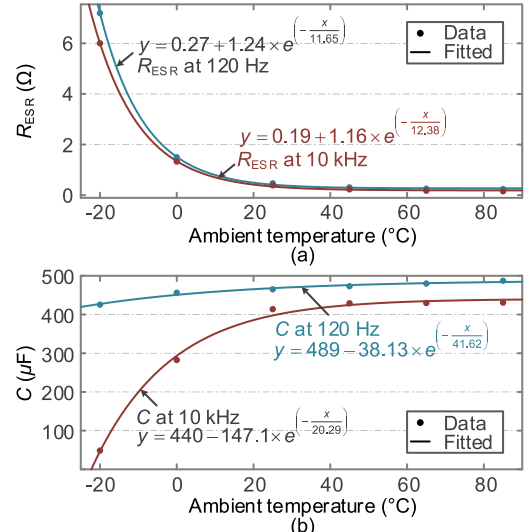


Fig. 5. R_{ESR} and C variations versus temperature of a new capacitor (Type: SLPX 470 μ F/ 450 V, datasheet [104]). (a) R_{ESR} versus temperature. (b) C versus temperature.

based on C is defined as [118]

$$C(t) = A_{\text{MPPF}} + \lambda_1 \cdot \lambda_2 \cdot e^{-(\lambda_1 \cdot t)} \quad (3)$$

where A_{MPPF} is a parameter which depends on C_0 , and λ_1 , and λ_2 depend on the component characteristics and the applied stresses. Similarly, the degradation model of MLC-Caps is [119]

$$C(t) = C_0 (1 - k \cdot \log t) \quad (4)$$

where k represents the maximum percent capacitance loss per decade hour, which is changed with the materials of capacitors. Taking the experimental results in [116], [118], and [119] as examples, Table II lists the experimental parameters of degradation models.

3) *Electrical Parameters Calibration*: It is noticed that the electrical parameters of capacitors are easily influenced by the operating frequency, ambient temperature, which needs to be calibrated in CM systems [120], [121]. Usually, the operating frequency of capacitors in converters is dependent on the known switching frequency, however, the ambient temperature is changing. Taking the Al-Cap (Type: SLPX 470 μ F/ 450 V) as an example, Fig. 5(a) and (b) shows R_{ESR} and C variations versus temperature, respectively [104], which are given from a manufacturer datasheet. It is found that C increases as the ambient temperature T_a increases and R_{ESR} decreases as T_a increases. The relationship between R_{ESR} , C of a new capacitor,

and ambient temperature is given as [59]

$$\begin{cases} R_{\text{ESR}}(T_a) = \alpha_{\text{AI}} + \beta_{\text{AI}} e^{-T_a/\gamma_{\text{AI}}} \\ C(T_a) = \chi_{\text{AI}} + \lambda_{\text{AI}} e^{-T_a/\nu_{\text{AI}}} \end{cases}, T_{\min} < T_a < T_{\max} \quad (5)$$

where α_{AI} , β_{AI} , γ_{AI} , χ_{AI} , λ_{AI} , and ν_{AI} are characteristics coefficients of capacitors, which are determined experimentally. T_{\min} and T_{\max} represent the minimum and maximum operating temperatures of capacitors, respectively, which are defined by the manufacturers. For SLPX-type capacitors, T_{\min} and T_{\max} are -40°C and $+85^{\circ}\text{C}$, respectively. Referring to Fig. 5, the variations of R_{ESR} and C at different frequencies are different. Therefore, it is needed to define the estimation frequency to establish the relationships in (5) before CM. Assuming the estimation frequencies of R_{ESR} and C are 10 kHz and 120 Hz, respectively, α_{AI} , β_{AI} , γ_{AI} , χ_{AI} , λ_{AI} , and ν_{AI} of this type of capacitor are 0.19, 1.16, 12.38, 489, -38.13, and 41.62, respectively. Notice that the relationship between C and T_a in (5) is based on the physical meaning of capacitors. It also can be written as $C(T_a) = \chi_{\text{AI}} + \lambda_{\text{AI}} \times T_a + \nu_{\text{AI}} \times T_a^2$ [56], which is based on the polynomial fitting. Here, χ_{AI} , λ_{AI} , and ν_{AI} are 448.5, 0.84, and -0.0049, respectively. Although the relationship between R_{ESR} , C , and T_a can be constructed, it is recommended to monitor the capacitors at a relatively low temperature (e.g., 25°C) due to the influence of degradation on R_{ESR} and C is not significant at high temperatures [31].

The capacitance C of MPPF-Caps and MLC-Caps is also influenced by the temperature. For MPPF-Caps, the effects of temperature on C are dependent on the capacitor materials. For polypropylene (PP) capacitors, C decreases as the ambient temperature increases. For polyethylene terephthalate (PET) and Polyethylene naphthalate (PEN) capacitors, C increases as the ambient temperature increases. Generally, the relationship between ambient temperature T_a and capacitance is [122]

$$C(T_a) = \alpha_{\text{MPPF}} \cdot C_{20^{\circ}\text{C}}(T_a - T_{\text{test}}) + C_{\text{test}} \quad (6)$$

where C_{test} and T_{test} are, respectively, the capacitance and temperature under the testing condition, $C_{20^{\circ}\text{C}}$ is the reference capacitance at 20°C , and α_{MPPF} is the temperature coefficient. α_{MPPF} of PP, PET, and PEN capacitors are $-250 \times 10^{-6}/\text{K}$, $600 \times 10^{-6}/\text{K}$, and $200 \times 10^{-6}/\text{K}$, respectively. Similarly, the relationships between ambient temperature T_a and capacitance of MLC-Caps can be constructed. Taking Class I MLC-CAs as an example, the relationship is [123]

$$C(T_a) = \alpha_{\text{MLC}} \cdot C_{\text{test}}(T_a - T_{\text{test}}) + C_{\text{test}} \quad (7)$$

where C_{test} represents the capacitance at T_{test} (i.e., 25°C). According to the result of data fitting [124], α_{MLC} is defined as 0.001629. For Class II and III ceramic capacitors, the relationship between C and T_a can also be constructed in the same way.

III. DERIVATION OF CM METHODS FOR DC-LINK CAPACITORS

Comparing with industrial instruments measurement based methods, the parameters estimation based methods are more economic, which can be implemented without impairing the power converter operation. Fig. 6 presents a derivation procedure

for parameters estimation methods of dc-link capacitors. The key steps are discussed as follows.

A. Parameters Estimation Principles

According to the dependence on the capacitor model, two main categories of principles are generally used to estimate the electrical parameters of dc-link capacitors. One is to estimate the parameters based on the capacitor impedance model, another is independent of the capacitor model. Furthermore, according to the type of needed electrical signals, the first category principle includes two subtypes, i.e., periodic small-signal ripples based principle (Principle I) and nonperiodic large-signal charging/discharging profiles based principle (Principle II). The second category principle treats the power electronic system as a black box, which does not need the specific capacitor model and converter model. Here, we define it as Principle III (i.e., black-box model).

Fig. 6(a) shows the equivalent circuit of dc-link capacitors, where v_{CAP} and i_C denote the voltage and current of capacitors, respectively. Based on Ohm's law, the capacitor voltage ripple Δv_{CAP} and capacitor current ripple Δi_C having the following relationship:

$$\begin{aligned} \Delta v_{\text{CAP}}(t) = & \frac{1}{C} \int_0^t i_C(t) dt + R_{\text{ESR}} \cdot \Delta i_C(t) \\ & + L_{\text{ESL}} \cdot \frac{di_C(t)}{dt}. \end{aligned} \quad (8)$$

Considering that L_{ESL} is very small (on the order of $10\text{--}100\text{ nH}$ [41]) at the working frequency of converters (i.e., low-and mid-frequency bands in Fig. 2), which can be ignored in dc-link capacitors. Hence, (8) can be written as

$$\Delta v_{\text{CAP}}(t) = \frac{1}{C} \int_0^t i_C(t) dt + R_{\text{ESR}} \cdot \Delta i_C(t). \quad (9)$$

Furthermore, Δv_{CAP} at low-frequency band and mid-frequency band can be simplified as

$$\Delta v_{\text{CAP_LF}}(t) \approx \frac{1}{C} \int_0^t i_{\text{C_LF}}(t) dt \quad (10)$$

$$\Delta v_{\text{CAP_MF}}(t) \approx R_{\text{ESR}} \cdot \Delta i_{\text{C_MF}}(t) \quad (11)$$

where $\Delta v_{\text{CAP_LF}}$, $\Delta i_{\text{C_LF}}$ denote the ripples at low-frequency band, and $\Delta v_{\text{CAP_MF}}$, $\Delta i_{\text{C_MF}}$ indicate them at mid-frequency band. From (10) and (11), C and R_{ESR} can be estimated as

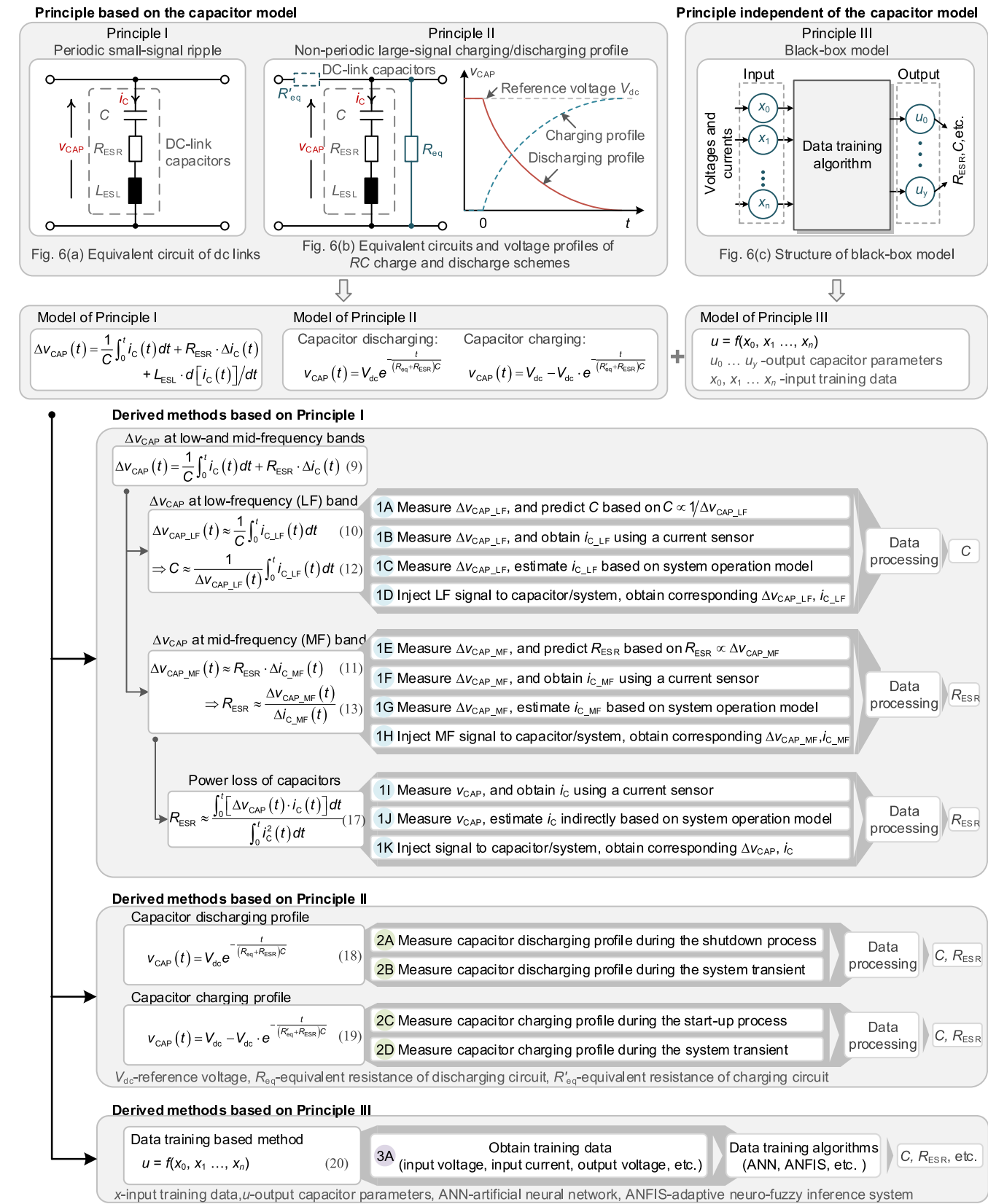
$$C \approx \frac{1}{\Delta v_{\text{CAP_LF}}(t)} \int_0^t i_{\text{C_LF}}(t) dt \quad (12)$$

$$R_{\text{ESR}} \approx \frac{\Delta v_{\text{CAP_MF}}(t)}{\Delta i_{\text{C_MF}}(t)}. \quad (13)$$

From (12) and (13), it is easily found that C is inversely proportional to the voltage ripple Δv_{CAP} and R_{ESR} is proportional to Δv_{CAP} for a given i_C . Hence, (12) and (13) can be simplified as (14) and (15) when i_C is given

$$C \propto 1/\Delta v_{\text{CAP_LF}} \quad (14)$$

$$R_{\text{ESR}} \propto \Delta v_{\text{CAP_MF}}. \quad (15)$$



Note: 1) The methods 1A and 1E, 1B and 1F, 1C and 1G, 1D and 1H can be grouped together respectively when using (9). Here, C and R_{ESR} are approximately estimated under the same frequency, such as low frequency or mid frequency.

2) Fig. 6(b), (18), and (19) are examples of Principle II. For different charging or discharging modes, the profiles and equations are different.

Fig. 6. Derivation procedure for parameters estimation methods of dc-link capacitors.

Referring to (11), the main power loss of capacitors is caused by R_{ESR} . Considering different harmonic frequencies, the total power loss P_{loss} of capacitors is

$$P_{\text{loss}} = \sum_{k=1}^n R_{\text{ESR},k} I_{C,\text{RMS},k}^2 \quad (16)$$

where $R_{\text{ESR},k}$ and $I_{C,\text{RMS},k}$ represent, respectively, the ESR and the root mean square (rms) current for each harmonic k [126]. Although (16) can be used to calculate ESR, it is difficult to determine $R_{\text{ESR},k}$ for each harmonic k . Moreover, the end-of-life criteria (e.g., $R_{\text{ESR}}/R_{\text{ESR}0} > 2$) provided by manufacturers are usually based on a frequency region (i.e., mid-frequency band) without considering a specified frequency. As discussed in [38], R_{ESR} calculated by the average power loss P_{loss} and the total rms current $I_{C,\text{RMS}}$ can approximately represent the actual ESR of capacitors in power electronic converters. Therefore, R_{ESR} is approximately calculated as

$$R_{\text{ESR}} \approx \frac{\bar{P}_{\text{loss}}}{I_{C,\text{RMS}}^2} = \frac{\int_0^t [\Delta v_{\text{CAP}}(t) \cdot i_C(t)] dt}{\int_0^t i_C^2(t) dt}. \quad (17)$$

Principle II is based on the large-signal discharging/charging profile, as shown in Fig. 6(b). The left part of Fig. 6(b) shows the equivalent circuit of capacitor discharging and charging schemes, where R_{eq} and R'_{eq} represent the equivalent resistances of discharging circuits and charging circuits, respectively. The right part gives the discharging and charging profiles, where V_{dc} denotes the reference value of capacitor voltage. During the discharging period, the capacitor voltage is expressed as

$$v_{\text{CAP}}(t) = V_{\text{dc}} e^{-\frac{t}{(R_{\text{eq}} + R_{\text{ESR}})C}}. \quad (18)$$

During the charging period, the capacitor voltage is

$$v_{\text{CAP}}(t) = V_{\text{dc}} - V_{\text{dc}} \cdot e^{-\frac{t}{(R'_{\text{eq}} + R_{\text{ESR}})C}}. \quad (19)$$

By solving (18) and (19), R_{ESR} and C can be estimated.

Principle III is based on the black-box model, as shown in Fig. 6(c). Here, the power electronic system to be monitored is treated as a black box. Taking the voltage and current signals of systems as input data, the capacitor parameters can be estimated using data training algorithms [e.g., artificial neural network (ANN)] without considering the specific capacitor model and converter model. The relationship between capacitor parameters and input signals can be obtained using training algorithms, i.e.,

$$u = f(x_0, x_1, \dots, x_n) \quad (20)$$

where $u_0 \dots u_y$ denote the output capacitor parameters, and $x_0, x_1 \dots, x_n$ are the input training data.

B. Derivation of CM Methods

Based on the three key principles, the CM methods for dc-link capacitors can be derived in a step by step manner. There exist 16 derived methods, as shown in Fig. 6.

1) *Derived Methods Based on Principle I:* There exist 11 derived methods based on Principle I, where methods 1A and 1E use the voltage ripple to approximately estimate the capacitor parameters without dependence on the capacitor current. The methods 1B–1D, 1F–1H, and 1I–1K utilize sampled or

estimated capacitor current to calculate R_{ESR} or C , which are illustrated using the examples in Fig. 7.

Fig. 7(a) shows an implementation example of methods 1B and 1F. Here, the capacitor current is directly sampled by a current sensor. To accurately obtain R_{ESR} or C , a band-pass filter and a low-pass filter are required, respectively. To avoid using capacitor current sensors, the methods 1C and 1G utilize the circuit operation model to indirectly obtain i_C . Referring to Fig. 7(b), taking a buck converter as an example, it is easily found that $i_C = i_L - i_o$, where i_L and i_o are inductor current and load current, respectively.

The implementation of schemes 1D and 1H can be divided into two categories. One is to inject current into the tested capacitor directly, as shown in Fig. 7(d). Here, a signal generation circuit including a signal generator and a power amplifier is employed to inject current signals at given frequencies to the tested capacitor. The injected signal can be sinusoidal waves, square waves, triangle waves, etc. Another is to inject a perturbation signal into the power electronic systems. Taking a PV grid-connected inverter as an example, Fig. 7(e) gives the implementation scheme. Here, a current at the h th harmonic frequency is injected into the grid, which causes the $(h-1)$ th and the $(h+1)$ th voltage and current ripples to appear on the dc-link capacitors. Then, R_{ESR} and C can be estimated using the voltage and current ripples at the $(h-1)$ th or the $(h+1)$ th.

Note that the methods 1A and 1E, 1B and 1F, 1C and 1G, 1D and 1H can be grouped together, respectively, when using (9). The description is listed in Table III. Here, C and R_{ESR} are approximately estimated under the same frequency, such as low frequency or mid frequency.

According to (17), R_{ESR} can be calculated using power losses of capacitors. Fig. 7(c) shows the implementation of the method II. It is similar to the method 1B, however, a band-pass filter is not required. The implementation of method 1J and 1K are similar to 1G and 1H, respectively.

2) *Derived Methods Based on Principles II and III:* There exist four derived methods based on Principle II, where 2A, 2B are based on the discharging profile, and 2C, 2D are based on the charging profile.

The methods 2A and 2C obtain the discharging or charging profiles during the shutdown process or start-up process of converters. Referring to Fig. 6(b), during the shutdown process of converter, the dc-link capacitors discharge through the equivalent resistor R_{eq} . The capacitor parameters can be estimated based on the discharging profile and (18). During the start-up process of converter, the capacitors charge through R'_{eq} . The capacitor parameters can be estimated based on the charging profile and (19). Taking modular multilevel converters (MMCs) as an example, the left part of Fig. 8(a) shows the circuit of a three-phase MMC, which include the detailed circuit of a submodule (SM) [127]. During the dc-side start-up process, the power switches S_1 turns OFF and S_a turns ON, the equivalent circuit of a signal-phase MMC is given in the right part of Fig. 8(a). Here, R_s and $R_{s,\text{eq}}$ represent the equivalent start-up resistance with/without considering the resistance of diodes, N denotes the number of SM in each arm, and C_i and R_i are the capacitance and resistance of the i th SM, respectively. Referring to the right part of Fig. 8(a), the capacitors are charged through

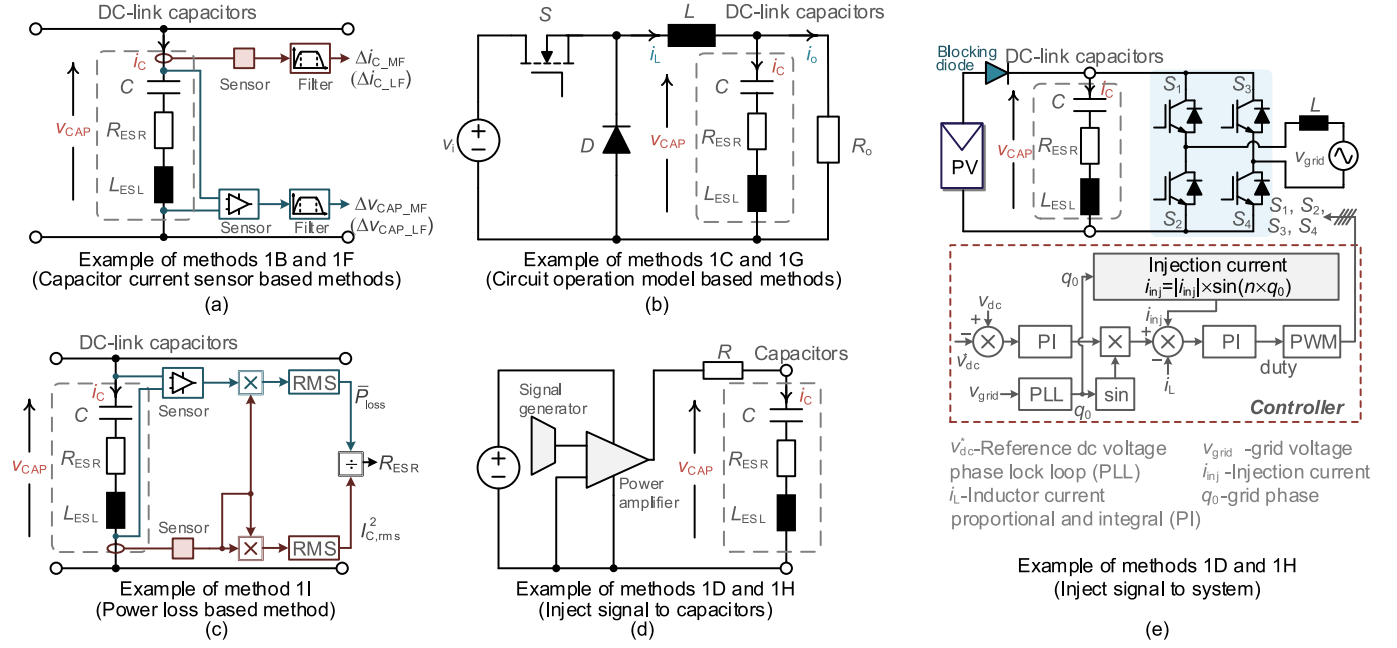


Fig. 7. Implementation examples of derived methods based on Principle I. (a) Example of methods 1B and 1F. (b) Example of methods 1C and 1G based on a buck converter. (c) Examples of methods II. (d) Example of method 1D and 1H, here, extra signals are injected to capacitors. (e) Example of method 1D and 1H based on a PV inverter, here, extra signals are injected to systems.

TABLE III
DESCRIPTION OF DERIVED METHODS 1A – 1H

Derived methods	Description
1A, 1E	Capacitor voltage based methods
1B, 1F	Capacitor current sensor based methods
1C, 1G	Circuit operation model based methods
1D, 1H	External signal injection based methods

R_{s_eq} during this start-up process. Assuming each SM has the same phase current i_{ph} and the same capacitor voltage v_{Ci} , the capacitances can be estimated using the equivalent dc voltage V_{dc_eq} , R_{s_eq} and the charging profile [see Fig. 6(b)].

Similar to the shutdown and start-up processes, the capacitors will be discharged or charged during transients. Taking buck converters as examples, Fig. 8(b) shows the voltage profile (i.e., capacitor charging profile) during an unloading transient. Based on the relationship between charging profile and capacitor parameters, R_{ESR} and C can be estimated [99].

The method 3A is based on Principle III, and an implementation example is shown in Fig. 8(c). Here, an ANN algorithm is used to estimate the capacitance for an ac/dc/ac system. Taking dc-link voltage and output current as training data, the capacitance can be estimated based on the data training algorithm.

C. Data Processing

Referring to Fig. 6, data processing is a key link of the CM for dc-link capacitors. Fig. 9 shows the general procedure of data processing for CM. First, the sampling signals are filtered using filtering, wavelet transform denoising (WTD), etc. Then, parameter estimation algorithms are employed to obtain capacitor parameters. For methods 1B, 1C, 1F, 1G, and 1K, the key issue

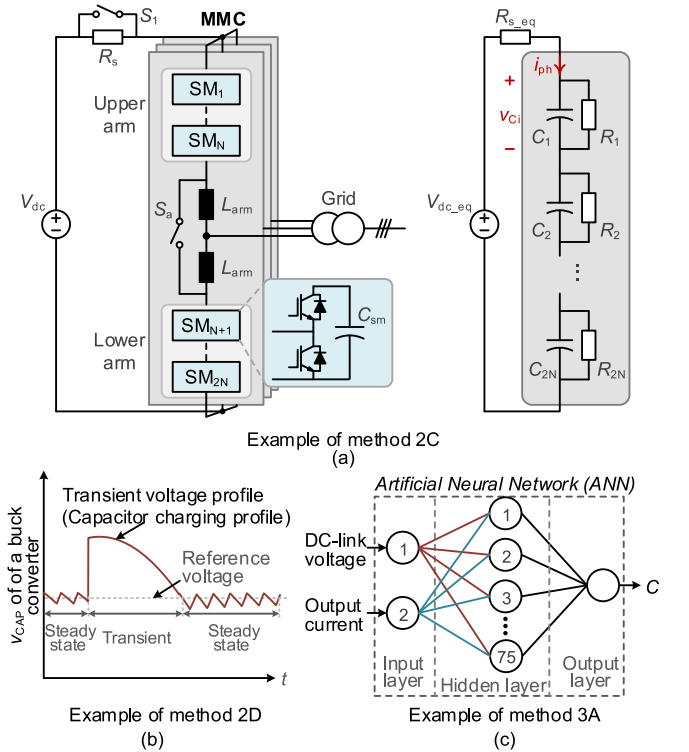


Fig. 8. Implementation examples of derived methods based on Principles II and III. (a) Example of method 2C based on an MMC. (b) Example of method 2D based on a buck converter. (c) Example of method 3A.

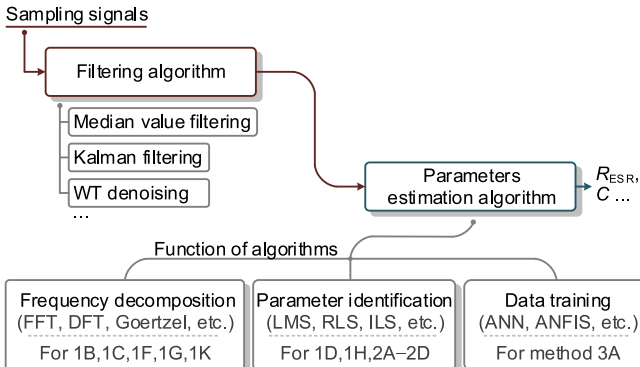


Fig. 9. Data processing procedure for CM.

is to obtain the low-frequency or mid-frequency components of capacitor voltage and capacitor current. Usually, frequency decomposition algorithms including fast Fourier transform (FFT) algorithm, discrete Fourier transform (DFT) algorithm, Goertzel algorithm, etc., are used to extract the low-frequency or mid-frequency components of v_{CAP} and i_C .

For methods 1D, 1H, and 2A–2D, adaptive filter algorithms including least mean squares (LMS) algorithm, recursive least squares (RLS) algorithm, iterative least squares (ILS) algorithm, etc. are widely used to identify R_{ESR} and C in (9)–(11), (18), and (19). Moreover, some optimization algorithms, such as particle swarm optimization (PSO) algorithm, genetic algorithm (GA) can be used to identify capacitor parameters.

For method 3A, data training algorithms including ANN algorithm, adaptive neuro-fuzzy inference system (ANFIS) algorithm, support vector regression (SVR) algorithm, etc., are widely used for CM.

IV. APPLICATION OF DERIVED CM METHODS

A. Overview of the Application of CM Methods

Based on the derived methods, various CM techniques for dc-link capacitors have been proposed in [11]–[109]. Fig. 10 gives the development history of these techniques. It is found that the research on the CM techniques for dc-link capacitors started at the end of the 1990s, and it has become a hot issue in the past decade.

Fig. 11(a) shows a statistical analysis of CM techniques for different types of dc-link applications, where the offline schemes estimate the capacitor parameters under the case that the capacitors are dismantled from converters, which can be applied for all types of converters. Different from offline schemes, real-online or quasi-online schemes (CM under special test conditions, such as start-up and shutdown process) can be implemented on-site in a real system, which are widely used for the CM of capacitors in ASD systems, PV inverters, PFC converters, dc/dc converters, etc.

From Fig. 11(a), it is found that the dc–dc converters and ac/dc/ac or dc/ac ASD systems are the most popular research

objectives. More than 60% of CM techniques are proposed for these two types of applications. For different dc-link applications, Fig. 11(b) gives the distribution of CM methods, where the ordinate shows the number of applied methods. Taking ASD systems and dc/dc converters as examples, it is found the signal injection based method (1D, 1H) and circuit operation model based method (1C, 1G) are widely used, respectively. Moreover, from the perspective of availability, Fig. 11(b) illustrates that the real-online scheme is the most popular one for CM.

For different types of dc-link applications, the detailed discussions of CM methods are given in Sections V to VII. Offline monitoring techniques are independent of topologies of converters, which are investigated in the following part.

B. Offline Monitoring Techniques

1) Implementation of Offline Monitoring Schemes: Generally, industrial instruments including LCR meter, impedance analyzer, etc., can be used for the offline measurement of R_{ESR} and C of capacitors. Considering the high price of these instruments, various low-cost offline measurement techniques have been presented in [11]–[24]. Ignoring L_{ESL} , a simple offline scheme is shown in Fig. 12(a).

Here, a sinusoidal signal is injected into an LC circuit, then R_{ESR} near the resonance frequency ω of an Al-Cap is estimated as [11], [12]

$$R_{\text{ESR}} = \sqrt{\left(\frac{v_{\text{CAP}} L_1 C \omega}{v_{\text{in}}}\right)^2 - \frac{1}{\omega^2}} / C \quad (21)$$

where v_{in} is the injected sinusoidal signal. However, this scheme ignores the effect of frequency on R_{ESR} and C .

To overcome the aforementioned shortcomings, Amaral and Cardoso [13]–[19] used an RC circuit to estimate the capacitor parameters. Referring to Fig. 12(b), a modulated sinusoidal signal is injected to the RC circuit, which causes sinusoidal voltage v_{CAP} and current i_C on the capacitor. According to the relationship between v_{CAP} and i_C , R_{ESR} and C can be estimated by using analysis algorithms, such as Laplace transform [13], Newton–Raphson (NR) algorithm [14], [15], DFT [16], [17], and LMS algorithm [18], [19].

Besides the sinusoidal signal generation circuit, a charge-discharge circuit is proposed in [19] and [20], as shown in Fig. 12(c). Using the LMS algorithm, the capacitor parameters are calculated based on the relationship between v_{CAP} and i_C . In [21] and [22], another RC circuit scheme is proposed, as shown in Fig. 12(d). Here, the injection signal is a square wave, which is different from that of Fig. 12(b). Using v_{CAP} and v_{in} , C and R_{ESR} are estimated at low-frequency and high-frequency bands, respectively. Referring to Fig. 12(e), a buck converter with a sinusoidal pulsewidth modulator is also proposed for offline measurement of capacitors [23]. Using DFT, R_{ESR} and C are calculated based on the analysis of v_{CAP} and i_C .

All of the above-mentioned schemes are implemented based on methods 1D and 1H. Different from that, Amaral and Cardoso [24] utilized the power loss on capacitors to estimate capacitor parameters. Referring to Fig. 12(b), a low-frequency sinusoidal current is injected into the capacitor, then R_{ESR} and C are

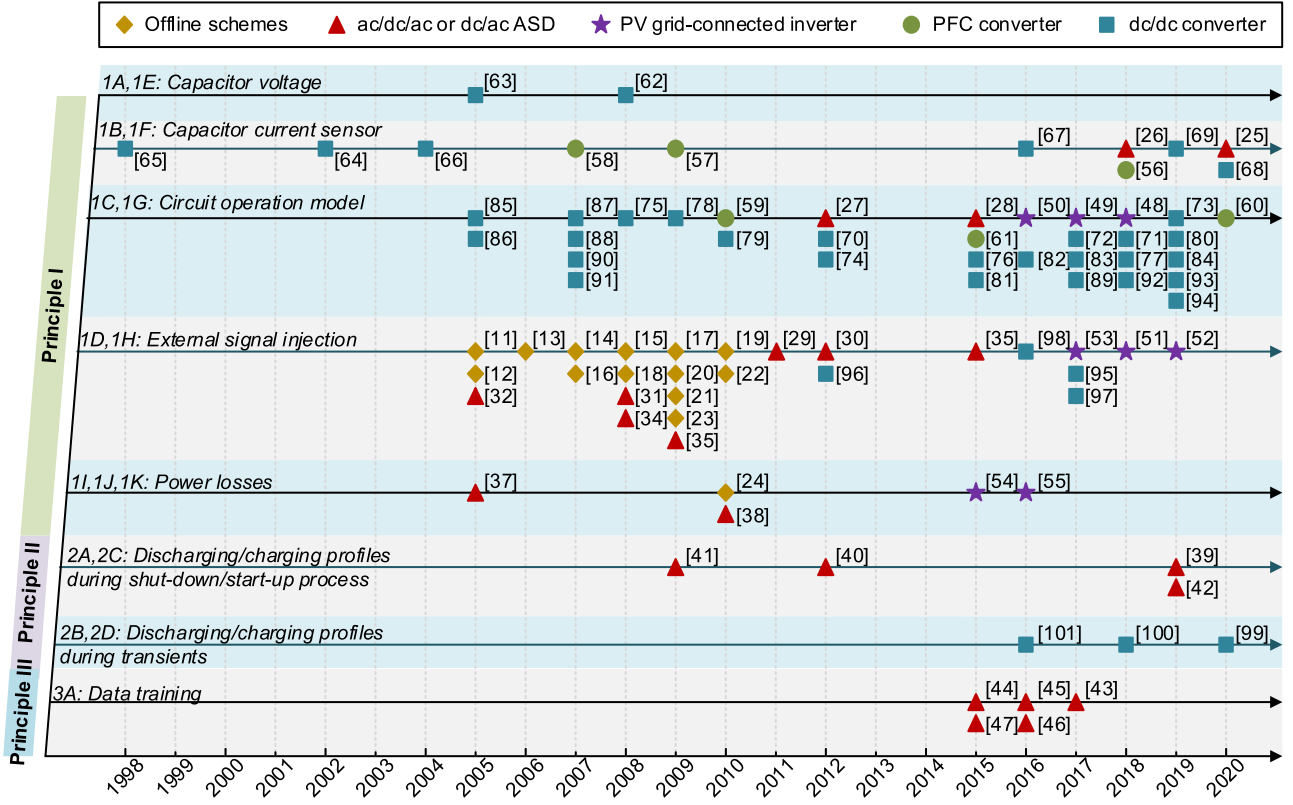


Fig. 10. Development history of the CM techniques for dc-link capacitors.

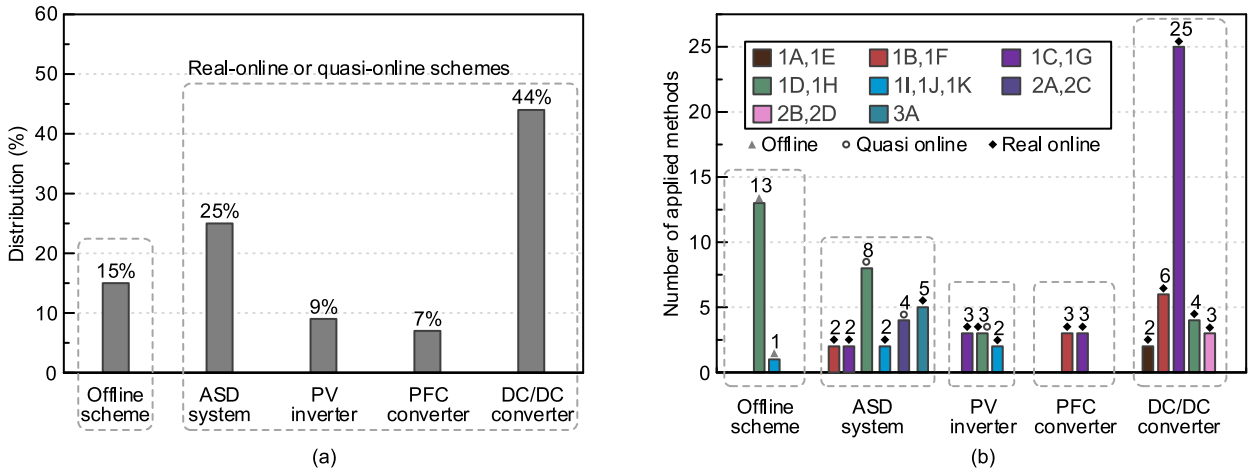


Fig. 11. Statistics of CM techniques for dc-link applications. (a) Statistics of research objects. (b) CM schemes for different types of dc-link applications.

calculated as

$$\begin{cases} R_{\text{ESR}} = \bar{P}T / \int_0^T i_C^2(t)dt \\ C = T / 2\pi \sqrt{\left(\int_0^T v_{\text{CAP}}^2(t)dt \right) / \left(\int_0^T i_C^2(t)dt \right) - R_{\text{ESR}}^2} \end{cases} \quad (22)$$

where T is the period of the sinusoidal signal and P is the capacitor average power.

2) *Discussion of Offline Monitoring Schemes:* As mentioned above, the offline schemes are mainly based on methods 1D, 1H, and 1K (i.e., signal injection scheme). Various data processing algorithms including Laplace transform, DFT, LMS, etc., are used. To compare the estimation accuracy of these algorithms, Table IV lists the estimation errors of C and R_{ESR} . Here, sinusoidal signal injection scheme [see Fig. 12(b)] is taken as examples. It illustrates that the estimation errors of the Laplace transform and NR algorithm are relatively high. And, the NR

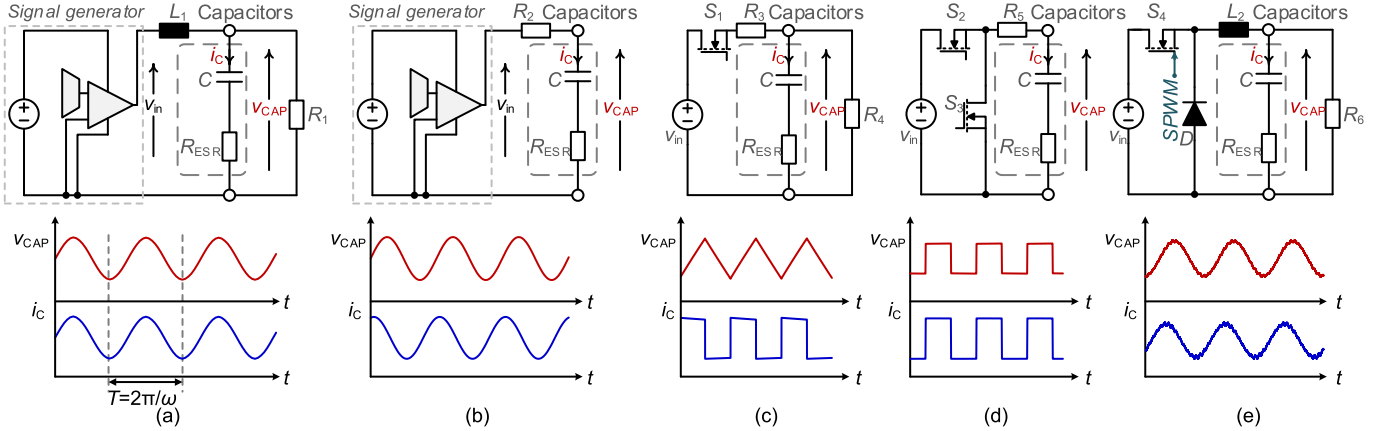


Fig. 12. Schematics of CM schemes for dismantled capacitors, here, L_{ESL} is ignored. (a) LC circuit with sinusoidal signal injection scheme. [12]. (b) RC circuit with sinusoidal signal injection scheme [13]–[19]. (c) Charge-discharge circuit scheme [19], [20]. (d) Square wave signal injection scheme [21], [22]. (e) Buck converter scheme [23].

TABLE IV

ESTIMATION ERROR OF SINUSOIDAL WAVE INJECTION CIRCUIT WITH DIFFERENT ALGORITHM

Injection signal	Methods	Algorithms	Error of $C \delta_C$	Error of $R_{ESR} \delta_R$	Ref.
Sinusoidal wave circuit [Fig. 12(b)]	1D, 1H	Laplace	$\delta_{C_120Hz}=17.6\%$	$\delta_{R_750Hz}=18\%$	[13]
		NR	$\delta_{C_120Hz}=1.5\%$	$\delta_{R_120Hz}=19.8\%$	[14]
		DFT	$\delta_{C_120Hz}=1.5\%$	$\delta_{R_1kHz}=5.9\%$	[17]
		LMS	$\delta_{C_120Hz}=0.8\%$	$\delta_{R_1kHz}=0.3\%$	[19]
1K		N/A	$\delta_{C_50Hz}=4.7\%$	$\delta_{R_50Hz}=3.5\%$	[24]

NR-Newton-Raphson algorithm, DFT-discrete Fourier transform algorithm, LMS-least mean square algorithm.

TABLE V

ESTIMATION ERROR FOR DIFFERENT TYPES OF SIGNAL-INJECTION CIRCUIT

Signal injection circuit	Algorithms	Error of $C \delta_C$	Error of $R_{ESR} \delta_R$	Ref.
Sinusoidal wave circuit [Fig. 12(b)]	LMS	$\delta_{C_120Hz}=0.8\%$ $\delta_{C_1kHz}=0.3\%$	$\delta_{R_120Hz}=1.6\%$ $\delta_{R_1kHz}=9.7\%$	[19]
Charge-discharge circuit [Fig. 12(c)]	LMS	$\delta_{C_120Hz}=1.9\%$ $\delta_{C_1kHz}=1\%$	$\delta_{R_120Hz}=4.1\%$ $\delta_{R_1kHz}=0.4\%$	[19]
Square-wave circuit [Fig. 12(d)]	N/A	$\delta_{C_1kHz}=4.9\%$	$\delta_{R_150kHz}=8.8\%$	[22]
Buck converter [Fig. 12(e)]	DFT	N/A	$\delta_{R_1kHz}=3\%$	[23]

LMS-least mean square algorithm, DFT-discrete Fourier transform algorithm.

algorithm is not suitable for the estimation of R_{ESR} . For the DFT algorithm and LMS algorithm, their estimation errors are relatively low and the error of the LMS algorithm is minimum.

To compare the estimation accuracy of different types of signal injection circuit, Table V summarizes the estimation error of these schemes. Due to the lack of data processing algorithms, the estimation accuracy of square-wave circuit [see Fig. 12(d)] is relatively low. For capacitance estimation, the estimation accuracy of sinusoidal wave circuit [see Fig. 12(b)] is larger than that for charge-discharge circuit [see Fig. 12(c)]. The estimation accuracy decreases as the injection-signal frequency increases. For an ESR estimation, the charge-discharge circuit [see Fig. 12(c)] has a relatively high estimation accuracy. The estimation error decreases as the injection-signal frequency increases.

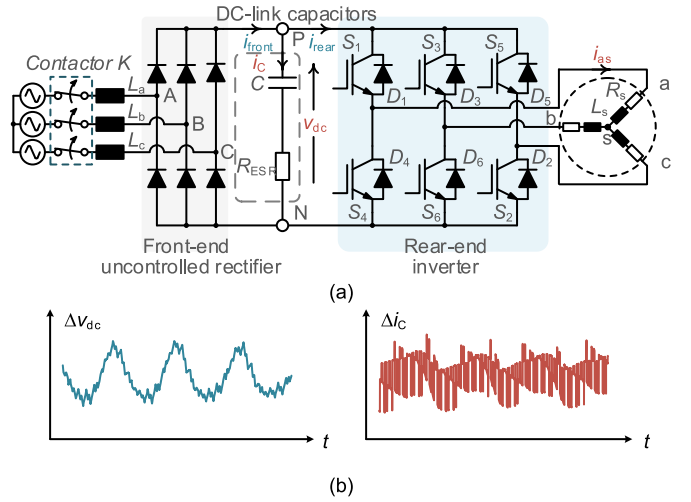


Fig. 13. ASD system with a front-end diode rectifier [26], here, L_{ESL} is ignored. (a) System structure. (b) Capacitor voltage ripple and current ripple.

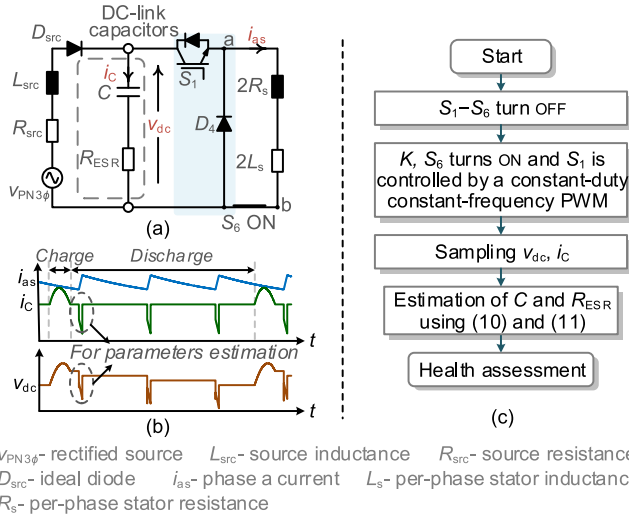
In summary, a low-frequency sinusoidal current injection based scheme is more suitable for the capacitance estimation. A square-wave current with relatively high frequency is more suitable for the ESR estimation.

V. CM FOR CAPACITORS IN AC/DC/AC OR DC/AC ASD SYSTEMS

ASD systems are widely used in industrial and residential applications. Various CM schemes for capacitors in ASD systems have been presented in [25]–[47].

A. Implementation of CM Schemes Based on Principle I

1) *Capacitor Current Sensor Based Methods (1B, 1F)*: A generic structure of two-stage ASD systems with a front-end diode rectifier is shown in Fig. 13(a). The corresponding dc-link voltage waveform and capacitor current waveform are shown in Fig. 13(b). In [25] and [26], a CM scheme based on 1B and 1F



$V_{PN3\phi}$ - rectified source L_{src} - source inductance R_{src} - source resistance
 D_{src} - ideal diode i_{as} - phase a current L_s - per-phase stator inductance
 R_s - per-phase stator resistance

Fig. 14. Current injection based scheme [29], here, L_{ESL} is ignored. (a) Equivalent circuit under CM condition. (b) Key waveforms. (c) Flowchart of the monitoring scheme.

is proposed to estimate the capacitor parameters of this system. First, the capacitor voltage ripple and current ripple are directly measured by sensors, as shown in Fig. 7(a). Then data processing algorithms, such as the Goertzel algorithm [25] and FFT [26] are applied to analyze the sampled waveforms. Based on (12) and (13), C and R_{ESR} are estimated using the extracted mid-frequency and low-frequency components of capacitor current ripple Δi_C and voltage ripple Δv_{CAP} .

2) *Circuit Operation Model Based Methods (1C, 1G)*: To avoid using a capacitor current sensor, Wechsler *et al.* [27] and Makdassi *et al.* [28] indirectly obtain capacitor current using $i_c = i_{front} - i_{rear}$, where i_{front} and i_{rear} represent the front-end current and rear-end current, respectively. Referring to Fig. 13(a), when $i_{rear} = 0$, i_c equals i_{front} . Based on the estimated capacitor current, R_{ESR} and C can be calculated using (12) and (13).

3) *External Signal Injection Based Methods (1D, 1H)*: In [29] and [30], a signal injection scheme is proposed to estimate the capacitor parameters of ASD systems. Referring to Fig. 13(a), CM is taken when the motor is stopped. Here, the contactor K is keeping ON. When S_6 is turned ON and S_1 is controlled by a constant-duty constant-frequency PWM, the charge on the capacitor can be discharged through the phase a and phase b windings, which causes voltage and current ripples on the dc link. The equivalent circuit and corresponding waveforms are given in Fig. 14(a) and (b), respectively. Using ripples Δv_{dc} and Δi_C , C and R_{ESR} can be estimated based on (10) and (11). The flowchart is shown in Fig. 14(c). In [31], the same method is used for a single-phase motor drive system.

Besides a diode rectifier, a pulsewidth modulation (PWM) converter is widely used as the first stage of two-stage ASD systems, as shown in Fig. 15(a). In [32]–[35], Dong-Choon *et al.* utilize current injection-based schemes to estimate the capacitor parameters of PWM converters [front end of Fig. 15(a)] and two-stage ac/dc/ac converters. Referring to Fig. 15(b), at no-load condition, a controlled ac current i_{inj} with a lower frequency (30 Hz) than the line frequency is injected into the front-end PWM

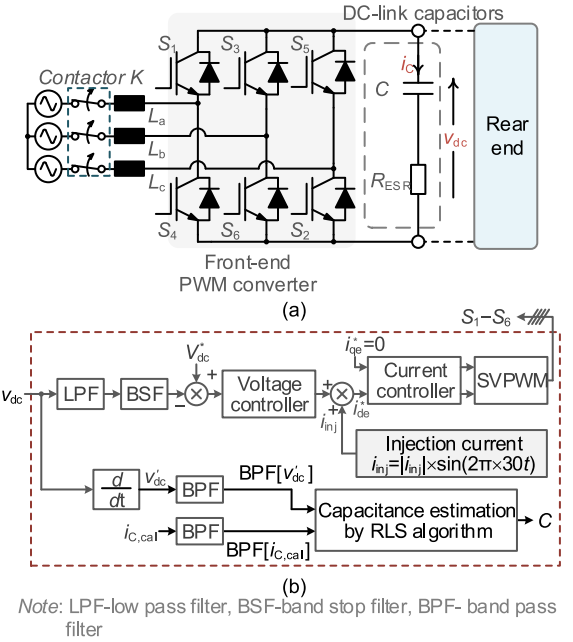


Fig. 15. Block diagram for monitoring capacitors in a PWM converter [32], here, L_{ESL} is ignored. (a) Structure of a PWM converter. (b) Block diagram of a signal injection based scheme.

converter, which induces voltage ripples on the dc link. Using (10) as well as the extracted v_{dc} and i_{dc} at 30 Hz, C is estimated based on the RLS algorithm [32], i.e.,

$$C = \frac{\text{BPF}[i_{C,cal}]}{\text{BPF}[v'_{dc}]} \quad (23)$$

where $\text{BPF}[\cdot]$ represents the band-pass filter quantity and $i_{C,cal}$ is the derived capacitor current based on the system operation mode.

Utilizing the similar schemes, the capacitor parameters of three-phase systems or single-phase systems are estimated in [33]–[35], where Pu *et al.* [33] were based on the current injection and Abo-Khalil and Lee [34] and Pu *et al.* [35] were based on the voltage injection. Notice that for an ASD system with a front-end uncontrolled rectifier, it is impossible to inject current signals into the front end at no-load condition. Therefore, Nguyen and Lee [36] injected the ac current signal into the rear-end inverter when the motor operates in the regenerative model.

4) *Power Losses Based Method (II)*: Based on the estimated method in Fig. 7(d), Aeloiza *et al.* [37] and Vogelsberger *et al.* [38] calculated R_{ESR} using $R_{ESR} = P_{dc,rms}/I^2 C_{rms}$. In [37], the rms values $P_{dc,rms}$, $I^2 C_{rms}$ were obtained using analog rms converters. In [38], the rms values were calculated in a microcontroller.

B. Implementation of CM Schemes Based on Principle II

Usually, the capacitor discharging profile is obtained during the shutdown process of systems. In [39], an auxiliary capacitor-discharge network is proposed for two-stage ac/dc/ac converters. Referring to Fig. 16(a), a variable electric network (VEN) consisting of auxiliary switches and resistors is connected in

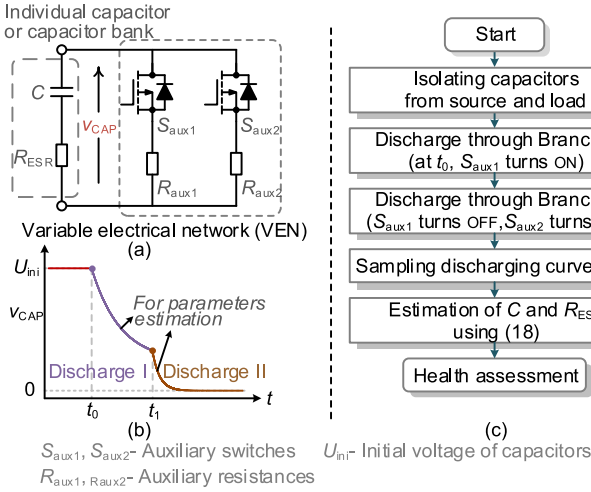


Fig. 16. Variable resistance network based capacitor discharge scheme [39], here, L_{ESL} is ignored. (a) Variable resistance network. (b) Discharge profile. (c) Flowchart of the monitoring scheme.

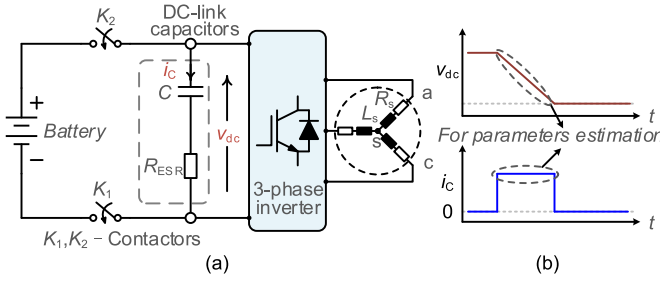


Fig. 17. Constant-current discharge based scheme [40], here, L_{ESL} is ignored. (a) Electrical configuration of an electric vehicle. (b) Constant-current discharge profiles.

parallel with dc-link capacitors (individual capacitor or capacitor bank). After the converter shuts down, the dc-link capacitors are isolated from the power source and load. The charge in capacitors can be released through the auxiliary resistor net. By controlling the switching of auxiliary switches S_{aux1} and S_{aux2} , a two-period discharge trajectory is formulated, as shown in Fig. 16(b). Sampling the discharge profile, C and R_{ESR} can be estimated based on (18). The flowchart is shown in Fig. 16(c).

Besides the additional discharging path, motor windings and impedance networks in the converter systems are used to form a discharge path. In [40], a constant-current discharge scheme is proposed to monitor the capacitors in the ASD system for electric vehicles. Referring to Fig. 17(a), when the motor is stopped, capacitors and inverter are isolated from the power source (K_1 and K_2 are opened). Here, the capacitors start to discharge through the windings. By controlling the inverter, the capacitors can discharge at a constant current, as shown in Fig. 17(b). Using the discharge profiles v_{dc} and i_C , the capacitance can be estimated using (18). In [41], an LC -resonance capacitor-discharge profile based scheme is proposed for an ASD system [see Fig. 13(a)]. The CM is taken when the system is before start up. Fig. 18(a) shows the equivalent circuit of the rear-end inverter under the capacitor monitoring condition. By turning ON

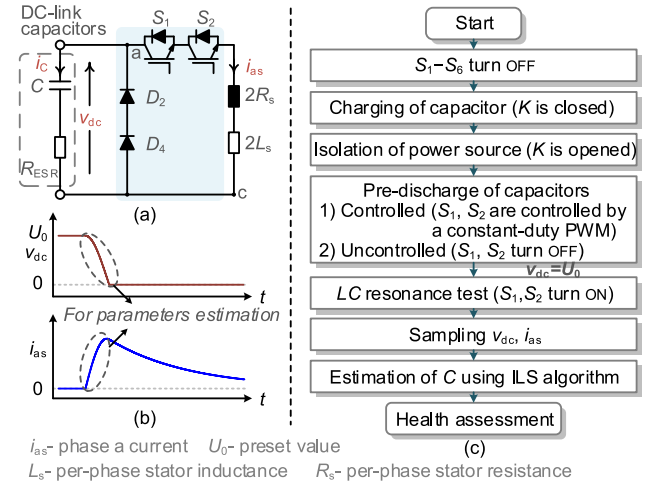


Fig. 18. LC -resonance based capacitor-charge scheme [41], here, L_{ESL} is ignored. (a) Equivalent circuit under CM condition. (b) Capacitor discharging profile. (c) Flowchart of the monitoring scheme.

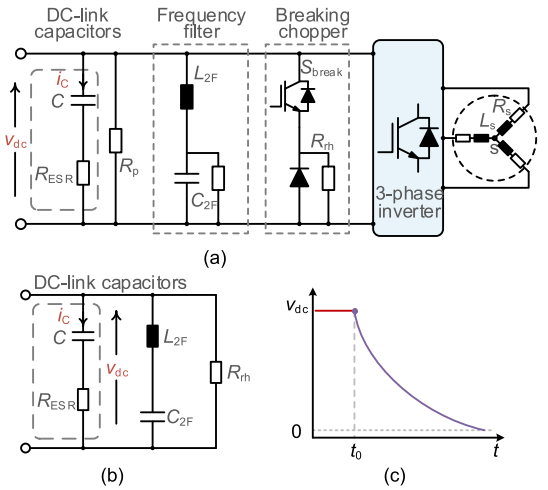


Fig. 19. Capacitor discharge through impedance networks in an ASD system for railway power trains [42], here, L_{ESL} is ignored. (a) Structure of a general traction scheme. (b) Equivalent circuit under CM condition. (c) Discharging profile.

S_1 and S_2 , the capacitor, phase a and phase c windings can form an LC -resonant circuit during the capacitor discharging period. The discharging profile is shown in Fig. 18(b). By sampling the discharging trajectories v_{dc} and i_{as} , the capacitance can be calculated by ILS algorithm. The detailed monitoring flowchart is shown in Fig. 18(c).

Considering the impedance networks in the converter systems, a discharging profile based scheme is proposed for ASD systems in railway power trains [42], as shown in Fig. 19(a). When the motor is stopped, the dc-link is isolated from the source and motor. By controlling the switch S_{break} , a $C-LC-R$ -type discharge path is formed, as shown in Fig. 19(b). According to the discharging profile in Fig. 19(c), C is estimated using the LMS algorithm.

TABLE VI
SUMMARY OF CM SCHEMES FOR CAPACITORS IN ASD SYSTEMS

Method	Working principle	Experimental error	Advantages	Limitations
Capacitor current directly measurement (1B, 1F)	[25]: A current sensor is used to sample capacitor current. Then use the Goertzel algorithm to extract low-frequency (300 Hz) and switching-frequency (2.5 kHz) ripples.	$R_{ESR} < 3\%$ $C < 1\%$	Real-online estimation.	Additional current sensors and filter circuits, complex algorithms.
	[26]: A current sensor is used to sample capacitor current. Then use fast Fourier transform (FFT) algorithm is used to analyze mid-frequency (15 kHz) ripples.	$R_{ESR} < 3.86\%$		
System operation model (1C, 1G)	[27], [28]: Utilizing the operation mode of converters to indirectly acquire capacitor current ripple and sampled voltage ripple to estimate C .	$C < 5.2\%$ [27]	Real-online estimation, no additional hardware circuit and current sensors.	Small-amplitude ripple measurement, estimated i_C .
Signal injection (1D, 1H)	[29]–[31]: The power switches are controlled to realize the charge and discharge (through the motor windings) of capacitors, then sample the constructed waveforms to estimate parameters.	$R_{ESR} < 2\%$ [31] $C < 5\%$ [31]	No additional hardware circuits and current sensors.	Quasi-online estimation, motor is stopped, additional control of switches, small-amplitude ripple measurement.
	[32]–[36]: Low-frequency ac current or voltage are injected to the front-end ac/dc converter [32]–[35] or rear-end dc/ac converter [36], then use the recursive least squares (RLS) algorithm or support vector regression (SVR) to analyze the corresponding voltage ripple to estimate parameters.	$R_{ESR} < 3.2\%$ [33] $C < 0.4\%$ [34]	No additional hardware circuits and current sensors.	Quasi-online estimation, external signal injection, operation in no load condition [32]–[35] or regenerative mode [36].
Power losses (II)	[37], [38]: R_{ESR} is calculated using average power losses of capacitors. Analog circuits [37] and an MCU [38] are used to calculate the power losses.	$R_{ESR} < 1.8\%$ [38]	Real-online estimation, no need for specific band-pass filter.	Additional capacitor current sensor [37], [38], extra power loss calculation circuit [38].
Discharging profile (2A)	[39]: Control capacitors discharge through a variable electric network (VEN), then estimate R_{ESR} and C using the discharging profile.	$R_{ESR} < 1.3\%$ $C < 0.047\%$	High estimation accuracy.	Quasi-online estimation, additional VEN on dc link, which introduces reliability risks, during shutdown process, need control of switches.
	[40]–[42]: Control capacitors discharge through the motor windings [40], [41] and electric network [42] in the converter, then estimate C using the discharging profile.	$C < 2.1\%$ [41]	No additional hardware circuits and current sensors.	Quasi-online estimation, motor is stopped, need control of switches [40], [41], electric vehicles application [40], railway trains application [42].
Data training (3A)	[43]–[46]: Using the artificial neural network (ANN) network to train data such as input voltage/current, output input voltage/current, and dc-link voltage to obtain C .	$C < 2\%$ [46]	Real-online estimation, no additional hardware circuit and current sensors.	Need a large amount of training data and complexly algorithms.
	[47]: Using adaptive neuro-fuzzy inference system (ANFIS) algorithm to train voltage data to obtain the capacitor health state.	N/A		

C. Implementation of CM Schemes Based on Principle III

In [43]–[46], ANN algorithm based schemes are proposed to estimate the capacitor parameters of the ASD system. An implementation example is given in Fig. 8(c). The key issue of these schemes is to obtain and define a suitable training dataset. To accurately obtain the relationship between capacitor parameters and input training data (such as input current, input voltage, dc-link voltage, output current, output voltage), different capacitance and load conditions must be considered in the training process. Besides the ANN algorithm, an ANFIS algorithm is employed to train data to monitor the capacitor health state in [47].

D. Discussions of CM Schemes for Capacitors in ASD Systems

Table VI summarizes the CM schemes for capacitors in ASD systems. Brief remarks are given as follows.

- 1) The derived schemes based on 1B, 1F, and 1I can real-online estimate capacitor parameters, however, capacitor current sensors, additional signal processing circuits, and complex algorithms are required [25], [26], [37], [38].
- 2) The derived schemes based on 1C and 1G can real-online estimate capacitor parameters without a capacitor current sensor. However, the estimation accuracy is relative low [27], [28].
- 3) The derived schemes based on 3A are real-online estimate schemes, which have relatively estimation accuracy. Additional sensors and hardware circuits are not required. However, complexly training algorithms and a

large amount of training data are required, which is the maximum challenge [43]–[47].

- 4) The derived schemes in [29]–[36] (based on 1D, 1H) and [40]–[42] (based on 2A) are quasi-online schemes, without additional current sensors and hardware circuits. The estimation accuracy is relatively high, however, some complex control of systems needs to be considered.

In summary, from the perspective of estimation accuracy and hardware cost, the schemes based on signal injection (1D, 1H), discharging profile (2A), and data training (3A) are recommended for CM of capacitors in ASD systems.

VI. CM FOR CAPACITORS IN PV GRID-CONNECTED INVERTERS AND PFC CONVERTERS

A. CM for Capacitors in PV Grid-connected Inverters

Single-phase inverters are widely used in PV systems to feed power from energy sources to the grid. Some CM schemes of capacitors in single-phase inverters are presented in [48]–[55]. All of these schemes are derived based on Principle I.

- 1) *Circuit Operation Model Based Methods (1C, 1G)*: In [48], a derived scheme based method 1C is proposed to estimate C of the input capacitor in a single-phase grid-connected PV H4 inverter, as shown in Fig. 20(a). Here, the average capacitor current i_C is calculated as $i_C = i_{pv} - i_{inv} = i_{pv} - i_L(S_1S_4 - S_2S_3)$, where $S_1 - S_4$ are the state of the switches. The estimated capacitor current and capacitor voltage waveform are shown in Fig. 20(b). The dc-link voltage is sampled at two special instants t_1 and t_2 , where average capacitor current equals to 0, i.e.,

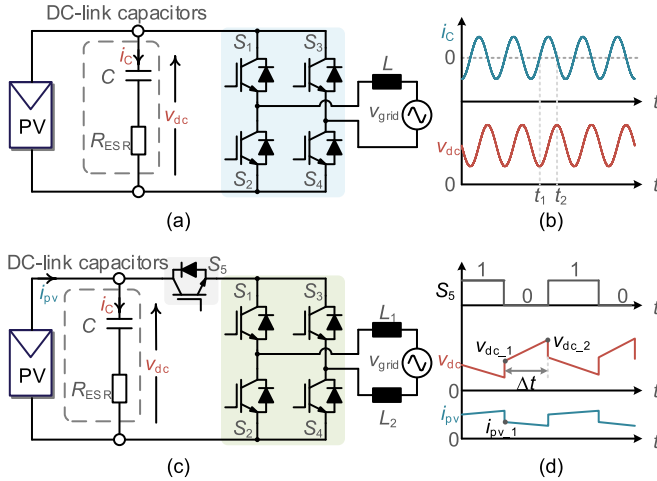


Fig. 20. Single-phase grid-connected PV H4 inverter [48] and H5 inverter [50]. (a) Structure of H4 inverter, here, L_{ESL} is ignored. (b) Average capacitor current and voltage waveforms. (c) Structure of H5 inverter. (d) Typical waveform of PV voltage and PV current in active and zero state.

$i_C(t_1) = i_C(t_2) = 0$. Thus, the capacitance is calculated using (12), i.e.,

$$C = \frac{\int_{t_1}^{t_2} i_C(t) dt}{v_{dc}(t_2) - v_{dc}(t_1)}. \quad (24)$$

Using the same capacitor current reconstruction method, Arya *et al.* [49] estimated the capacitor impedance at second harmonic frequency of a PV inverter as $Z_2 = V_{dc,2}/I_{C,2}$, where $V_{dc,2}$ and $I_{C,2}$ represent the rms values at second harmonic frequency.

In [50], a CM scheme is proposed for a PV H5 inverter, as shown in Fig. 20(c), the capacitance is calculated during the zero state, i.e., the power switch S_5 is turned OFF, as shown in Fig. 20(d). Using (10), C is calculated as $C = (i_{pv,1} \times \Delta t)/(v_{dc,2} - v_{dc,1})$.

2) *External Signal Injection Based Methods (1D, 1H)*: In [51], a current injection scheme is proposed for a grid-connected PV inverter, as shown in Fig. 7(e). Here, the CM of capacitors is taken during the night. At night, there is no voltage on the PV panel/string. Here, a current at the h th harmonic frequency is injected into the grid, which causes the $(h-1)$ th and the $(h+1)$ th voltage and current ripples to appear on the dc-link capacitors. Using (9), R_{ESR} and C can be estimated using the voltage and current ripples at the $(h-1)$ th or $(h+1)$ th based on the LMS algorithm. Utilizing the same monitoring scheme, Gupta *et al.* [52] further proposed a health estimation method for individual capacitors in a capacitor bank.

In [53], a short-circuit test scheme is introduced to a dc/ac converter to estimate R_{ESR} of capacitors, as shown in Fig. 21. Before the short-test, the converter operates in a normal state. Here, S_2 , S_3 are ON and S_1 , S_4 are OFF. At t_0 , S_1 turns ON, a very short time short-circuit test occurs, which causes a capacitor voltage step ΔV_{dc} . According to (11), R_{ESR} is calculated as $R_{ESR} = \Delta V_{dc} / I_{sc}$, where I_{sc} is the short-circuit current.

3) *Power Losses Based Method (1J)*: Based on the idea of power losses (i.e., method 1J), Arya *et al.* [54] and Agarwal *et al.* [55] proposed a power extraction efficiency (PEE) method

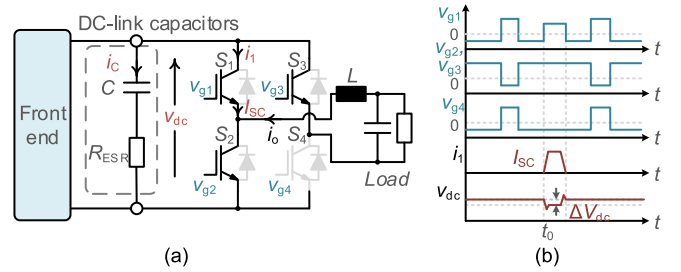


Fig. 21. Short-circuit current perturbation for capacitor monitoring in a single-phase inverter [53], here, L_{ESL} is ignored. (a) Equivalent circuit of a single-phase inverter during short-circuit test. (b) Short-circuit test waveforms.

to monitor the health state of capacitors. The PEE is defined as $PEE = P_{av}/P_{max}$, where P_{av} and P_{max} represent the average PV power and maximum PV power, respectively. By sampling the PV voltage and current, the PEE is calculated to estimate the health state of capacitors.

4) *Discussions of CM Schemes for Capacitors in the PV Inverter*: Table VII summarizes the CM schemes for capacitors in PV inverters, the remarks are given as follows.

- a) The CM schemes for capacitors in PV inverters are all based on Principle I.
- b) The signal injection scheme in [51] (based on 1D, 1H) is a quasi-online scheme, which has a relatively high estimation accuracy. However, the CM is implemented during the night and an additional power diode is required. Another injection scheme in [53] is a real-online scheme, which has high applicability. However, the estimation accuracy of R_{ESR} is relatively low, and high-frequency sampling of short-circuit current is required.
- c) The power losses schemes in [54] and [55] (based on 1J) and capacitor current estimation scheme in [49] (based on 1C, 1G) can real-online monitor the health status of capacitors without additional hardware circuits and current sensors. However, specially defined failure criteria are required.
- d) The capacitor current estimation scheme in [49] and [50] (based on 1C, 1G) are real-online schemes without additional hardware circuits and current sensors. However, the work in Agarwal *et al.* [50] is only suitable for PV H5 inverter, which has a low applicability.

In summary, from the perspective of estimation accuracy and hardware cost, the scheme in [48] was recommended for CM of capacitors in PV inverters.

B. CM for Capacitors in PFC converter

PFC converters are widely used in ac/dc conversion to improve the power factor (PF) and reduce the total harmonic correction. The CM schemes in [56]–[61] are designed for PFC converters, which are derived based on Principle I.

1) *Capacitor Current Sensor Based Methods (1B, 1F)*: Taking a boost PFC converter as an example, Fig. 22(a) shows its topology structure and key waveforms. In [56], C and R_{ESR} of capacitors are estimated using (10) and (11). Here, Prony's algorithm is used to process the sampled voltage and current data.

TABLE VII
SUMMARY OF CM SCHEMES FOR CAPACITORS IN PV GRID-CONNECTED INVERTERS AND PFC CONVERTERS

Topology	Method	Working principle	Experimental error	Advantages	Limitations
PV inverter	System operation model (1C, 1G)	[48]: Using estimated i_C and capacitor voltage to calculate C . The capacitor voltage is sampled in particular instants ($i_C=0$).	$C: <2.56\%$	Real-online estimation, no additional hardware circuits and current sensors.	Estimated i_C .
		[49]: Using the second harmonic voltage and current to calculate capacitor impedance.	$Z: <17.2\%$		Estimated i_C , low estimation accuracy, no specific values of R_{ESR} and C , specially defined failure criterion.
		[50]: Sampling capacitor voltage and PV current to calculate C when H5 inverter is worked in zero states, here, the capacitor is disconnected with the inverter.	N/A		Small-amplitude ripple, only suitable for H5 inverter.
	Signal injection (1D, 1H)	[51]: A low-frequency current harmonic is injected into the grid, which causes corresponding-frequency voltage ripple on capacitors. Using the least mean square (LMS) algorithm to analyze the ripple to estimate capacitor parameters.	$R_{ESR}: <3.65\%$ $C: <1.88\%$	No additional sensors.	Quasi-online estimation, no input source (at night), additional diode, external signal injection.
		[53]: Using the voltage step caused by a short-circuit test to estimate R_{ESR} .	$R_{ESR}: <6\%$		Causing switches in short-circuiting status, high-frequency sampling during the short test.
	Power losses (1J)	[54],[55]: Sampling PV voltage and current to calculate power extraction efficiency (PEE) to assess the health state of capacitors.	N/A	Real-online estimation, no additional hardware circuits and current sensors.	No specific values of R_{ESR} and C , specially defined failure criterion.
PFC converter	Capacitor current directly measurement (1B, 1F)	[56],[57]: Using a current sensor to sample capacitor current. Then use Prony's algorithm [56], discrete Fourier transform (DFT) algorithm [57] to analyze voltage and current ripples at low frequency and mid frequency.	$R_{ESR}: <6.01\%$ [56] $C: <2.51\%$ [56]	Real-online estimation.	Additional hardware circuits and sensors, high-frequency sampling.
		[58]: Using a current sensor to sample capacitor current. Then use the root mean square (RMS) values of capacitor voltage and current to calculate R_{ESR} .	$R_{ESR}: <5.5\%$		
	System operation model (1C, 1G)	[59]: Reconstruction of the capacitor current using diode current, then estimate capacitor parameters using Kalman filter.	$R_{ESR}: <5\%$ $C: <10\%$	Real-online estimation, no additional capacitor current sensor.	Low estimation accuracy, high-frequency sampling ($f_{sa}/f_{sw} = 16$).
		[60]: Using the ripple voltage step value at switch turn-off moment to estimate R_{ESR} . Wavelet transform (WT) algorithm is used to calculate the parameter.	$R_{ESR}: <9.5\%$		Low estimation accuracy, additional hardware circuits, high-frequency sampling ($f_{sa}/f_{sw} \approx 53$).
		[61]: Sampling of two values of the capacitor voltage in particular instants within a line cycle.	$R_{ESR}: <3.7\%$ $C: <1.9\%$		Additional hardware circuit.

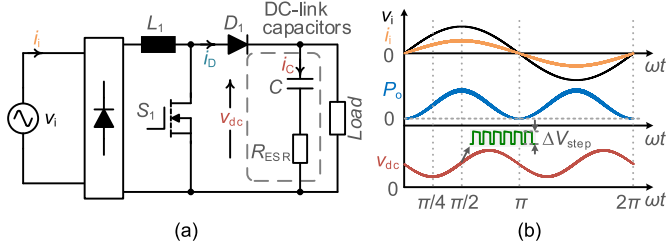


Fig. 22. Topology structure and key waveforms of boost PFC converters, here, L_{ESR} is ignored [60]. (a) Topology structure. (b) Key waveforms.

Similar, DFT is used in [57]. Moreover, according to (11), Imam *et al.* [58] calculated R_{ESR} using $R_{ESR} = V_{dc,RMS}/I_{C,RMS}$, where $V_{dc,RMS}$, and $I_{C,RMS}$ are the rms values of Δv_{CAP} and Δi_C , respectively.

2) *Circuit Operation Model Based Methods (1C, 1G):* Referring to Fig. 22(a), the capacitor current can be approximately calculated as $i_C = i_D - I_D \approx i_L \times \text{PWM} - \text{avg}(i_L \times \text{PWM})$, where I_D is the average diode current. Based on this, Abdennadher *et al.* [59] used Kalman filter algorithm, (10) and (11) to estimate C and R_{ESR} . Referring to Fig. 22(b), at $\pi/2$ in a half-line cycle, the peak value of the capacitor current is maximum, which causes the peak value of the voltage ripple to be maximum. According to (11), the ripple voltage step value ΔV_{step} is determined by R_{ESR} when the switch S_3 turns OFF. Therefore, Lu *et al.* [60] estimated R_{ESR} using $R_{ESR} \approx \Delta V_{step}/\Delta i_{L,\max}$, where $\Delta i_{L,\max}$

is the maximum value of inductor current ripple. Here, wavelet transform (WT) algorithms are used to calculate R_{ESR} .

The scheme in [60] analyzed the steady-state waveforms on the switching-frequency scale. Considering the line-frequency scale of a boost PFC, Yao *et al.* [61] used the capacitor voltage at 0 and $\pi/4$ instants to estimate capacitor parameters. According to the input and output power balance, R_{ESR} and C are calculated as (25), where V_{dc} is the average capacitor voltage

$$\begin{cases} R_{ESR} = -V_{dc} \times \Delta v_{dc}(0)/P_o \\ C = \frac{-P_o}{2\omega V_{dc} \Delta v_{dc}(\pi/4)} \end{cases} \quad (25)$$

3) *Discussions of CM Schemes for Capacitors in PFC Converters:* Table VII also summarizes the CM schemes for capacitors in PFC converters, the remarks are given as follows.

- The schemes are all real-online schemes, which are based on Principle I.
- The capacitor current directly measurement schemes in [56]–[58] (based on 1B, 1F) and capacitor current estimation schemes in [60] and [61] (based on 1C, 1G) required additional current sensors or hardware circuits to obtain capacitor current. Moreover, the schemes in [56]–[58], [60] require high-frequency sampling to achieve ripple signals.
- The capacitor current estimation schemes in [59] do not require additional current sensors, however, the estimation accuracy is relatively low.

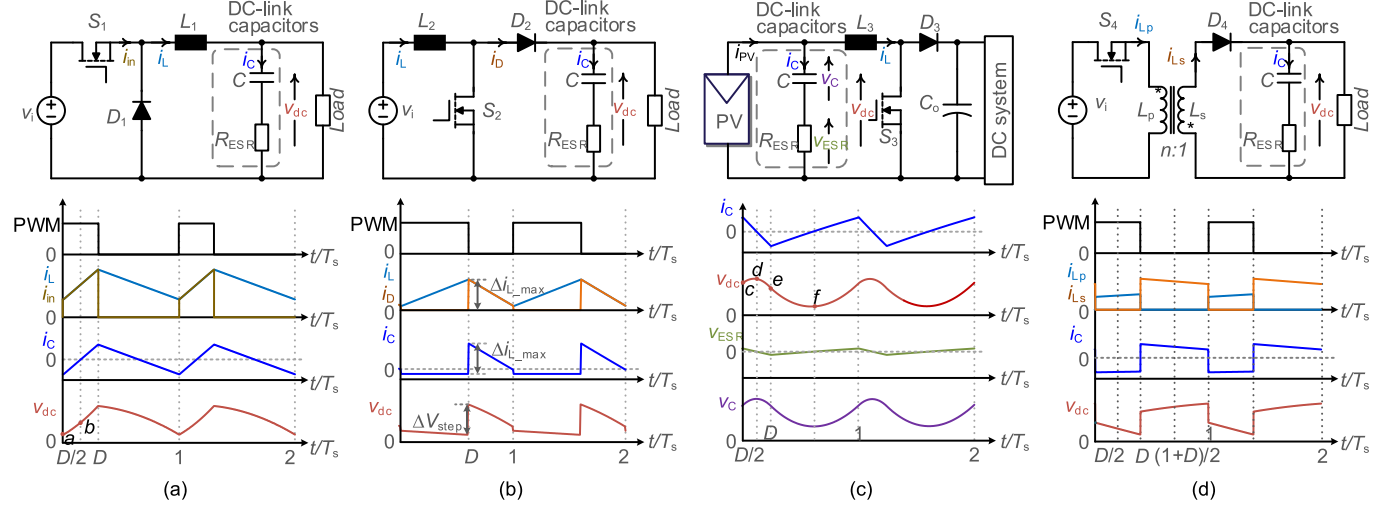


Fig. 23. Topology structure and steady-state waveforms of dc/dc converters, here, L_{ESL} is ignored. (a) Buck converter. (b) Boost converter. (c) PV boost converter. (d) Flyback converter.

VII. CM FOR CAPACITORS IN DC/DC CONVERTERS

Different from the ac/dc converters or dc/ac inverters, dc/dc converters have a relatively high switching frequency, which are widely used in low-power applications. In [62]–[101], a lot of CM schemes were proposed to assess the health status of capacitors in dc/dc converters.

A. Implementation of CM Schemes Based on Principle I

1) *Capacitor Voltage Based Methods (1A, 1E)*: Fig. 23(a) shows the main circuit and key waveforms of a buck converter. It illustrates that the output voltage waveform v_{dc} is similar to the capacitor current waveform i_C , which demonstrates that voltage ripple v_{dc} is proportional to R_{ESR} in (15). Based on this, Chen *et al.* [62] presented an analog circuit to extract the peak-to-peak value of voltage ripple, so as to predict the failure of capacitors in buck converters. In [63], a similar scheme is applied for a boost converter, as shown in Fig. 23(b).

2) *Capacitor Current Sensor based Methods (1B, 1F)*: In [64]–[69], the schemes based 1B and 1F are proposed for monitoring capacitors in forward converters [64], [65], flyback converters [66], buck converters [67], and PV boost converters [68], [69]. Here, C and R_{ESR} are calculated using (10) and (11), the implementation is shown in Fig. 7(a).

There are three types of current sensor are used to obtain capacitor current, i.e., the classical current sensor including shunt resistor and Hall sensor [64]–[66], printed circuit board Rogowski coil (PCBRC) sensor [67], tunnel magnetoresistive (TMR) sensor [68], [69], where the classical current sensor is invasive type, the PCBRC sensor, and TMR sensor are noninvasive type.

3) *Circuit Operation Model Based Methods (1C, 1G)*: In [70]–[94], circuit operation model based schemes are proposed for dc/dc converters. Generally, they can be divided into two categories. One is based on the converter operation model, here, the capacitor current is derived from inductor current, output current, and output voltage, etc. These signals are directly

measured by sensors. Another is based on converter parameters model, here, the signals are estimated from converter parameters by using circuit model.

a) *Based on the operation model of converters*: Referring to the waveforms of buck converters in Fig. 23(a), it is easily found that the inductor current ripple Δi_L equals to the capacitor current ripple Δi_C . Based on this, Wang *et al.* [70]–[73] estimated R_{ESR} using (13), i.e.,

$$R_{\text{ESR}} \approx \frac{\Delta v_{\text{dc}}}{\Delta i_C} = \frac{\Delta v_{\text{dc}}}{\Delta i_L}. \quad (26)$$

From Fig. 23(a), it is also found that the inductor current is related to the input current i_{in} . Therefore, Amaral and Cardoso [74], [75] used i_{in} to estimate R_{ESR} . To avoid using current sensors, Yao *et al.* [76], [77] sampled the capacitor voltage at two particular instants (points a and b) of one switching cycle to estimate R_{ESR} and C . As shown in Fig. 23(a), the difference between the capacitor voltages sampled at points a and b is due to R_{ESR} and C . Using (9), the estimation model is calculated as (27), where T_s and D represent the switching cycle and duty cycle, respectively. Here, to sample the voltage at points a and b , PWM signal is needed

$$\begin{cases} R_{\text{ESR}} = \frac{2L_1 f_s [\Delta v_{\text{dc}}(0) + 2 \frac{2(D-1)}{(2-D)} \times \Delta v_{\text{dc}}(\frac{D T_s}{2})]}{V_{\text{dc}}(D-1)} \\ C = \frac{V_o(2-D)(D-1)}{24 L_1 f_s^2 \Delta v_{\text{dc}}(\frac{D T_s}{2})}. \end{cases} \quad (27)$$

Referring to the waveforms of boost converters in Fig. 23(b), the inductor current i_L is proportional to the capacitor current i_C . Therefore, Amaral and Cardoso [78]–[80] used inductor current to estimate capacitor parameters. In [79] and [80], the LMS and the WTD algorithms are employed, respectively.

According to the steady-state waveforms of a continuous conduction mode (CCM) PV boost converter in Fig. 23(c), the difference between the capacitor voltages sampled at points c and e are due to R_{ESR} . The voltage difference at points d and f is only due to C . Using (9), R_{ESR} and C are calculated as (28),

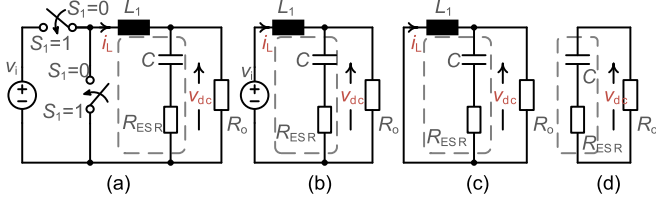


Fig. 24. Equivalent circuits of buck converter [85]. (a) Main circuit. (b) State 1. (c) State 2. (d) State 3.

where V_{dc} is the average capacitor voltage [81]

$$\begin{cases} R_{ESR} = [v_{dc}(0) - v_{dc}(DT_s)] L_2 / (V_{dc} DT_s) \\ C = \frac{V_{dc} DT_s^2}{8L_2 \{v_{dc}(DT_s/2) - v_{dc}[(1+D)T_s/2]\}}. \end{cases} \quad (28)$$

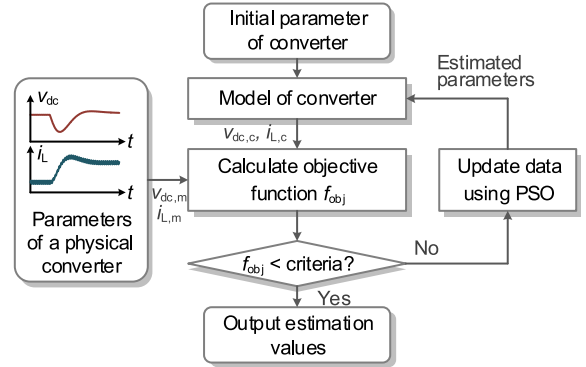
Based on this, Ahmad *et al.* [82] further proposed an improved estimation scheme to monitor the capacitors for a converter operated in discontinuous conduction mode (DCM). In [83], a similar scheme is proposed for a CCM flyback converter, as shown in Fig. 23(d). Based on the derivation of (9), the capacitor parameters are calculated using the output voltage at 0, $DT_s/2$, and $(1+D)T_s/2$. In [84], an improved multiple-spot sampling method is proposed for a DCM flyback converter.

b) Based on the circuit parameters model of converters: Since a power electronic circuit is a hybrid dynamic system, its operation can be described by a state-space model. In [85] and [86] a circuit model based method is proposed to estimate the capacitor parameters of a buck converter. Ignoring the ESL, Fig. 24(a) shows the equivalent circuit of the converter. The buck converter has two discrete states in CCM with (S_1, S_2) in the set $\{(1,0), (0,1)\}$, and three states in DCM with (S_1, S_2) in the set $\{(1,0), (0,1), (0,0)\}$, as shown in Fig. 24(b)–(d). Synthesizing these states with different values of switches, we have

$$\begin{aligned} \begin{bmatrix} i_L(t) \\ v_{dc}(t) \end{bmatrix} &= \begin{bmatrix} 1 & 0 \\ 0 & 1 - \frac{T}{(R_{ESR} + R_o)C} \end{bmatrix} \begin{bmatrix} i_L(t-1) \\ v_{dc}(t-1) \end{bmatrix} \\ &+ S_1(t-1) \begin{bmatrix} v_i/L \\ \frac{R_{ESR} R_o v_i T}{(R_{ESR} + R_o)L} \end{bmatrix} \\ &+ [S_1(t-1) + S_2(t-1)] \\ &\times \begin{bmatrix} 0 & -T/L \\ \frac{R_o T}{(R_{ESR} + R_o)C} & -\frac{R_{ESR} R_o T}{(R_{ESR} + R_o)L} \end{bmatrix} \begin{bmatrix} i_L(t-1) \\ v_{dc}(t-1) \end{bmatrix} \end{aligned} \quad (29)$$

where T is the sampling period. Using variables to represent the elements in the parameter matrixes in (29), it can be rewritten as

$$\begin{aligned} \begin{bmatrix} i_L(t) \\ v_{dc}(t) \end{bmatrix} &= \begin{bmatrix} a_{11} & a_{12} \\ a_{21} & a_{22} \end{bmatrix} \begin{bmatrix} i_L(t-1) \\ v_{dc}(t-1) \end{bmatrix} + S_1(t-1) \begin{bmatrix} b_1 \\ b_2 \end{bmatrix} \\ &+ [S_1(t-1) + S_2(t-1)] \begin{bmatrix} h_{11} & h_{12} \\ h_{21} & h_{22} \end{bmatrix} \begin{bmatrix} i_L(t-1) \\ v_{dc}(t-1) \end{bmatrix}. \end{aligned} \quad (30)$$



$v_{dc,m}$ -measured output voltage $i_{L,m}$ -measured inductor current $i_{L,c}$ -calculated inductor current $v_{dc,c}$ -calculated output voltage

Fig. 25. Flowchart of circuit model based PSO algorithm [93].

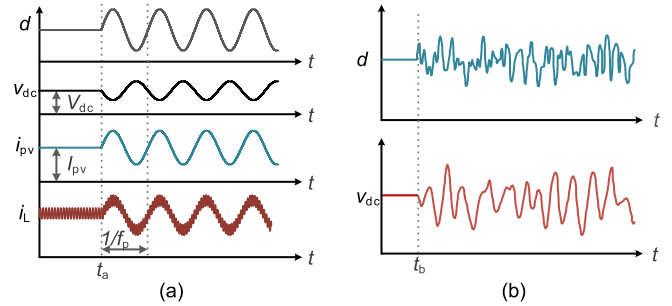


Fig. 26. Representative waveforms of duty cycle perturbation based schemes. (a) Waveforms of a PV boost converter [95]. (b) Waveforms of a buck converter [97].

According to (29) and (30), the capacitor parameters can be calculated as

$$\begin{cases} \hat{C} = (T \times \hat{R}_o - \hat{b}_2 \times \hat{L}_1 / v_i) / [(\hat{a}_{21} + \hat{h}_{21}) \times \hat{R}_o] \\ \hat{R}_{ESR} = \hat{b}_2 \times \hat{L}_1 / [v_i \times \hat{C} \times (\hat{a}_{21} + \hat{h}_{21})]. \end{cases} \quad (31)$$

Using the LMS algorithm, the coefficients $a_{11} \sim a_{22}, h_{11} \sim h_{22}$, b_1, b_2 , and capacitor parameters can be calculated. The similar methods are proposed for buck converters [87]–[90] and boost converters [91], [92].

Based on the circuit model, a PSO algorithm is used to estimate the circuit parameters include L , C , R_{ESR} , etc., as shown in Fig. 25 [93], [94]. Here, the output voltage $v_{dc,m}$ and inductor $i_{L,m}$ during load transient are target values of the PSO algorithm. If the calculated values $v_{dc,c}$ and $i_{L,c}$ are matched with the target values, the estimated converter parameters are consistent with the nonelectrical parameters. Based on this, the capacitor parameters can be obtained.

4) External Signal Injection Based Methods (1D, 1H): In [95], a signal injection method is proposed for a PV boost converter [see Fig. 23(c)]. Referring to Fig. 26(a), at t_a , a small perturbation signal of low frequency f_p is added to the original duty cycle d , which causes low-frequency oscillations on the voltage v_{dc} and current i_{pv} , i_L . Using (9), the low-frequency

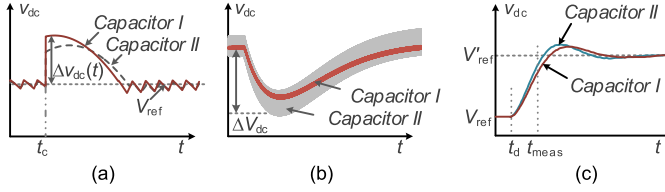


Fig. 27. Capacitor charging/discharging profiles during transients. (a) Transient waveforms of a buck converter [99]. (b) Transient waveforms of a full-bridge converter [100]. (c) Transient waveforms of a phase-shifted ZVS converter [101].

impedance of the capacitor is calculated as

$$Z_C(f_p) = V_{dc,rms}^{f_p} / I_{C,rms}^{f_p} \quad (32)$$

where $V_{dc,rms}^{f_p} / I_{C,rms}^{f_p}$ are the rms values of capacitor voltage and current at f_p . Here, the capacitor current i_C is calculated as $i_C = i_{pv} - i_L$. Similar duty-cycle perturbation methods and Principle IV are utilized for a buck converter [see Fig. 23(a)] in [96]–[98], where the discrete transfer function of the buck converter is given as

$$G_{dv}(z) = \frac{b_1 z^{-1} + b_2 z^{-2}}{1 + a_1 z^{-1} + a_2 z^{-2}}. \quad (33)$$

Referring to the duty cycle and output voltage waveforms in Fig. 26(b), before t_b , the converter works in a steady state. At t_b , a pseudo-random binary sequence (PRBS) perturbation is injected into the duty cycle, which causes an oscillation on the voltage v_{dc} . Using signal processing algorithms include infinite impulse response (IIR) filter [96], self-tuned Kalman filter [97], and biogeography-based optimization (BBO) [98] to analyze the duty cycle and voltage waveforms during perturbation period, the coefficients a_1, a_2, b_1, b_2 as well as capacitor parameters are identified.

B. Implementation of CM Schemes Based on Principle II

During transients, the capacitor will charge or discharge, which forms a charging or discharging profile. In [99], a load transient trajectory analysis based scheme is proposed for monitoring the output capacitor of a buck converter. Taking an unloading transient as an example, Fig. 27(a) shows the transient trajectories of capacitor voltage. Here, two capacitors with different parameters are used. It is found that the output voltage trajectory Δv_{dc} is changed as the output capacitor parameters change when the load current step ΔI_o is the same. Based on the charging profile, R_{ESR} and C are calculated as

$$\begin{cases} R_{ESR} = \Delta v_{dc}(t_c) / \Delta I_o \\ \Delta v_{dc}(t) = \frac{\Delta I_o}{C} t - \frac{1}{2} \frac{C}{k} t^2 + \Delta I_o \cdot R_{ESR} - R_{ESR} \cdot k t \end{cases} \quad (34)$$

where t_c is the initial instant of load step, k is the inductor current slew rate, and $k \approx V_{ref} / L_1$. In this scheme, an RC differential circuit is used to detect the load transient [125]. In [100], a similar method is proposed for a full-bridge converter. But the accurate mathematical relation between capacitor parameters and transient trajectory is not given, R_{ESR} is estimated as

$R_{ESR} \approx \Delta V_{dc} / \Delta I_o$, where ΔV_{dc} is the voltage deviation, as shown in Fig. 27(b).

Besides the load transient, a reference voltage perturbation scheme is proposed for a phase-shifted full-bridge converter in [101]. Referring to Fig. 27(c), at t_d , the reference voltage is modified as V'_{ref} , which causes a voltage step. For different capacitors, the voltage values at t_{meas} are different. By fitting the measurement data, C is estimated as follows:

$$C = \frac{148.2 - S + 0.1687 I_o}{27960} \quad (35)$$

where I_o is the load current and S represents the step slope and is related to the measurement value at t_{meas} .

C. Discussions of CM Schemes for Capacitors in DC/DC Converters

Table VIII summarizes the CM schemes for capacitors in dc/dc converters. It is found that the derived schemes are all real-online schemes, which are based on I Principle I and II. The remarks are given as follows.

- 1) It is known that dc/dc converters usually work with a relatively high switching frequency, which introduces high-frequency small-amplitude ripples. For the schemes based Principle I, high frequency and high-precision sampling devices are generally required to obtain steady-state ripples. And, powerful data processing tools are needed for filtering and analysis of sampling signals.
 - a) The derived schemes based on 1A and 1E (i.e., capacitor voltage based schemes) can predict the health status of capacitors without capacitor current sensors [62], [63]. However, there are no specific values of R_{ESR} and C , which is difficult to calculate RUL of capacitors. Moreover, Chen *et al.* [62] used analog circuit to judge the parameter change of capacitors, which does not need high-frequency sampling.
 - b) The derived schemes based on 1B and 1F in [64]–[69] have relatively high estimation accuracy (the estimation error is about 5%), however, capacitor current sensors and high-frequency sampling devices are required.
 - c) The converters operation model schemes (based on 1C, 1G) estimate R_{ESR} and C using the relationship between voltage ripple and current ripple. In [70]–[75], [80], high-frequency sampling devices are required. The schemes in [76]–[77] and [81]–[84] do not need high-frequency sampling devices, and the calculation model is simple. However, additional hardware circuits are required.
 - d) The circuit model schemes (based on 1C, 1G) in [85]–[92] also need high-frequency sampling to accurately obtain the circuit parameters model. Besides capacitor parameters, these schemes can estimate other key parameters, such as inductance. However, the calculation algorithm is complex and the estimation accuracy is relatively low. The schemes in [93] and [94] avoided high-frequency sampling, however, the estimation algorithm is also complex.

TABLE VIII
SUMMARY OF CM SCHEMES FOR CAPACITORS IN DC/DC CONVERTERS

Method	Topology	Working principle	Experimental error	Advantages	Limitations
Capacitor voltage based method (1A,1E)	buck	[62]: Using analog circuits to extract the dc value of ripple voltage, which can represent the change of R_{ESR} .	N/A	Real-online failure prediction, simple.	Additional ripple processing circuits, no specific values of R_{ESR} and C .
	buck	[63]: Fast Fourier transform (FFT) is used to analyze the estimated voltage ripple. Then, judge the parameter change of capacitors.	N/A		
Capacitor current directly measurement (1B,1F)	forward [64], [65] Flyback [66]	[64]–[66]: Using a current sensor to sample capacitor current, then calculate R_{ESR} based on switching-frequency voltage ripple and current ripple.	$R_{ESR} < 2.77\%$ [66]	Real-online estimation.	Additional capacitor current sensor, high-frequency sampling.
	buck	[67]: PCB Rogowski coil (RC) sensor is designed to capture capacitor current to estimate R_{ESR} .	$R_{ESR} < 5.56\%$	Real-online estimation, switch fault diagnosis.	Specially designed PCBRG sensor, high-frequency sampling.
	PV boost	[68], [69]: Magnetoinductive sensors are used to sample capacitor current to calculate R_{ESR} and C .	$R_{ESR} < 4.9\%$ [68] $C < 5.4\%$ [68]	Real-online monitor of input/output capacitors.	Special current sensor, high-frequency sampling.
Operation model of converters (1C,1G)	buck	[70]: Empirical mode decomposition (EMD) algorithm on capacitor voltage and inductor current.	N/A	Real-online estimation, no capacitor current sensor.	High-frequency sampling, complex algorithm.
	buck	[71]: Wavelet transform denoising (WTD) algorithm on ripple voltage and inductor current.	$R_{ESR} < 3.89\%$	Real-online estimation, consider DCM model, no additional capacitor current sensor.	High-frequency sampling ($f_{sw}/f_{sw}=2247$), complex algorithm.
	buck	[72],[73]: Calculation of R_{ESR} utilizing capacitor voltage and inductor current, where ripple current is extracted using Rogowski Coil (RC) sensor.	$R_{ESR} < 6\%$ [72]	Real-online estimation, switch fault diagnosis, no capacitor current sensor.	Specially designed RC sensor, high-frequency sampling.
	buck	[74],[75]: Utilizing the input current and the output voltage to estimate R_{ESR} , discrete Fourier transform (DFT) and least mean square (LMS) algorithms are used to compute the best values.	$R_{ESR} < 4.9\%$ [74]	Real-online estimation, no capacitor current sensor.	High-frequency sampling ($f_{sw}/f_{sw}=100$).
	buck	[76],[77]: Sampling voltage ripple at two particular instants of one switching cycle, calculation of R_{ESR} and C using pulse width modulation signal and voltage ripple.	$R_{ESR} < 7.6\%$ [76] $C < 6.37\%$ [76]	Real-online estimation, low-frequency sampling, no capacitor current sensor.	Addition hardware circuit.
	boost	[78],[79]: Capacitor current is indirectly obtained based on inductor current. Least mean square (LMS) algorithm is used.	$R_{ESR} < 10.5\%$ [79] $C < 15.8\%$ [79]	Real-online estimation, no capacitor current sensor.	High-frequency sampling ($f_{sw}/f_{sw}=100$ [79]), low estimation accuracy.
	boost	[80]: Capacitor current is indirectly obtained based on inductor current. Wavelet transform denoising (WTD) algorithm is employed.	$R_{ESR} < 3.06\%$	Real-online estimation, no capacitor current sensor.	High-frequency sampling ($f_{sw}/f_{sw}=333$).
	PV boost	[81],[82]: Using capacitor voltages of particular instants to calculate R_{ESR} and C .	$R_{ESR} < 6.2\%$ [82]	Real-online estimation, low-frequency sampling, no capacitor current sensor.	Addition hardware circuit.
	flyback	[83], [84]: Sampling voltage ripple at particular instants of one switching cycle, calculation of R_{ESR} and C using pulse width modulation signal and voltage ripple.	$R_{ESR} < 5.83\%$ [83] $C < 9.5\%$ [83]	Real-online estimation, low-frequency sampling, no capacitor current sensor.	Addition hardware circuit.
Circuit parameters model of converters (1C,1G)	buck	[85]–[88]: Using hybrid model as well as recursive least squares (RLS) algorithm and least mean square (LMS) algorithm to estimate capacitor parameters.	$R_{ESR} < 6.5\%$ [88] $C < 5.5\%$ [88]	Real-online estimation, no capacitor current sensor, full parameters monitoring.	High-frequency sampling ($f_{sw}/f_{sw}=25$), complex calculation model.
	PV buck	[89]: Using an adaptive model observe method to estimate C .	$C < 5\%$	Real-online estimation, no capacitor current sensor, full parameters monitoring.	High-frequency sampling ($f_{sw}/f_{sw}=660$), complex calculation model.
	boost	[90],[91]: Using hybrid model and least mean square (LMS) algorithm to estimate capacitor parameters.	$R_{ESR} < 13.3\%$ [91] $C < 7.5\%$ [91]	Real-online estimation, no capacitor current sensor, full parameters monitoring.	High-frequency sampling ($f_{sw}/f_{sw}=200$), complex calculation model.
	boost	[92]: Using modified hybrid model and wavelet transform denoising (WTD) algorithm to estimate capacitor parameters.	$R_{ESR} < 11.7\%$ $C < 9.2\%$	Real-online estimation, no capacitor current sensor, full parameters monitoring.	High-frequency sampling, complex calculation model.
	buck	[93],[94]: Taking the transient voltage and current as the target values, using particle swarm optimization (PSO) algorithm and circuit model to estimate the circuit parameters.	$C < 9.2\%$ [94]	Real-online estimation, no capacitor current sensor, full parameters monitoring.	Complex algorithm, estimation during transient.
Signal injection (1D, 1H)	PV boost	[95]: Injecting low-frequency perturbation signal (120 Hz) to duty cycle, then calculate the low-frequency impedance.	$Z < 0.64\%$	Real-online monitor, no capacitor current sensor.	External signal injection, additional circuits, no specific values of R_{ESR} and C .
	buck	[96]–[98]: Pseudo-random binary sequence (PRBS) is injected into the duty cycle, then estimate circuit parameters using infinite impulse response (IIR) filter [96], Kalman filter [97], and biogeography-based optimization (BBO) [98].	$R_{ESR} < 10.9\%$ [98] $C < 18.6\%$ [98]	Real-online estimation, no additional hardware, full parameters monitoring.	Complex algorithm, not suitable for high-frequency converter.
Discharging/charging profiles during transients (2B,2D)	buck	[99]: Using the large-signal load transient trajectory to estimate R_{ESR} and C .	$R_{ESR} < 7.4\%$ $C < 9.6\%$	Real-online estimation, low-frequency sampling.	Estimation during transient, additional hardware circuit.
	full-bridge converter	[100]: Using the maximum voltage deviation during load transient to estimate R_{ESR} .	N/A	Real-online estimation, low-frequency sampling.	Estimation during transient, no specific values of R_{ESR} and C .
	full-bridge converter	[101]: Modifying the reference voltage to introduce a voltage step, then estimate C using the voltage step.	N/A	Real-online estimation.	External signal perturbation, need offline training of data.

- e) The calculation model of the signal injection scheme (based on 1D, 1H) in [95] is simple and the sampling frequency is low. However, a simple ripple extraction circuit is required, and there are no specific values of R_{ESR} and C . The schemes in [96]–[98] can implement full parameters monitoring of converters. But complex algorithms limit their application in high-frequency converters.
- 2) The discharging/charging profiles schemes (based on 2B, 2D) avoid the high-frequency sampling of ripples. However, there is no data processing algorithms, which causes a relatively low estimation accuracy.
- 3) Taking a buck converter as an example, Table IX shows the comparison results of these derived schemes, where f_{sw} is the switching frequency and N represents the number of sampling points during one switching cycle. It illustrates

TABLE IX
COMPARISON OF CM SCHEMES FOR CAPACITORS IN BUCK CONVERTERS

Method	Additional circuits/ sampling devices	f_w (N)	Algorithm (complexity)	Experimental error
Capacitor voltage based method (1A)	Simple hardware circuits	50 kHz (N/A)	N/A	N/A [62]
Capacitor current measurement (1B, 1F)	Current sensor, oscilloscope	100 kHz (N=100)	N/A	$R_{ESR} < 5.56\%$ [67]
System operation model (1C,1G)	Oscilloscope	44.5 kHz (N=2247)	WTD (+++)	$R_{ESR} < 3.89\%$ [71]
	Oscilloscope	20 kHz (N=100)	LMS (++)	$R_{ESR} < 4.9\%$ [74]
	Simple circuits	100 kHz (N=2)	N/A	$R_{ESR} < 7.6\%$ [76] C: <6.37% [76]
System circuit model (1C,1G)	Acquisition card	20 kHz (N=150)	LMS (++)	$R_{ESR} < 6.7\%$ [85] C: <6% [85]
	Acquisition card	300 kHz (N=666)	N/A	C: <5% [89]
Signal injection (1D, 1H)	N/A	20 kHz (N=1)	BBO (+++)	$R_{ESR} < 10.9\%$ [98] C: <18.6% [98]
Charging profiles (2D)	Simple hardware circuits	200 kHz (N=1)	N/A	$R_{ESR} < 7.4\%$ [104] C: <9.6% [104]

TABLE X
SUMMARY OF THE CM SCHEMES WITHOUT ADDITIONAL CIRCUITS, SENSORS,
AND HIGH-FREQUENCY SAMPLING DEVICES

DC-Link application	CM method	Implementation	Experimental error	Ref.
AC/DC/AC or DC/DC ASD system	System operation model (1C, 1G)	Real online	C <5.2%	[27]
	Signal injection (1D, 1H)	Quasi online	$R_{ESR} < 2\%$ [31] C: <0.4% [34]	[29]–[36]
	Discharging profile (2A)	Quasi online	C: <2.1% [41]	[40]–[42]
	Data training (3A)	Real online	C: <2% [46]	[43]–[47]
PV inverter	System operation model (1C, 1G)	Real online	C: <2.56%	[48]
PFC converter	System operation model (1C, 1G)	Real online	$R_{ESR} < 5\%$ C: <10%	[59]
DC/DC converter	Circuit parameters model of converters (1C,1G)	Real online	C: <9.2% [94]	[93], [94]
	Signal injection (1D, 1H)	Real online	$R_{ESR} < 10.9\%$ [98] C: <18.6% [98]	[96]–[98]

that the derived schemes based on capacitor current direct measurement (1B, 1F) and circuit operation model (1C, 1G) generally require high-cost sampling devices, such as data acquisition card, which limits their application in industrial systems. Moreover, complex algorithms of signal injection (1D, 1H) based scheme limit their application for high-frequency dc/dc converters.

In summary, from the perspective of implementation, the charging/discharging profiles based schemes with low sampling frequency and data are recommended for CM of capacitors in dc/dc converters. Simple data processing algorithms can be considered to improve the estimation accuracy.

VIII. CONCLUSION

CM of dc-link capacitors has great significance in enhancing the reliability of the power electronics converters with dc link. In this article, an overview of CM techniques for dc-link

capacitors is presented. First, the wear-out failure characteristics of capacitors including degradation models and end-of-life criteria are summarized. Based on this, the design procedure of CM for dc-link capacitors is presented. Second, the main estimation principles of capacitor parameters are reviewed. Accordingly, the CM methods for dc-link capacitors are derived in a step by step manner. Third, the existing CM methods for dc-link capacitors are reviewed and discussed according to different types of dc-link applications including ASD systems, PV inverters, PFC converters, and dc/dc converters. Based on this literature review, Table X summarizes the existing CM schemes without additional hardware circuits, sensors, and high-frequency sampling devices. Moreover, the suggested feasible solutions for industrial applications are listed in the following. Future research challenges and research opportunities are summarized from the authors' point of view.

A. Suggested Feasible Solutions

The key goal of employing a CM scheme in industrial applications is to accurately estimate capacitor parameters without additional cost and reliability risk, i.e., without additional hardware circuits and sensors. For the application with charging or discharging paths, such as ASD systems (motor windings as discharging paths). The best solution for CM of capacitors is to construct discharging or charging profile during shutdown or start-up processes (i.e., schemes based on 2A, 2C); then, to analyze the charging/discharging profile to estimate capacitor parameters.

- For the application without charging or discharging paths, such as PV inverters, and PFC converters, circuit operation model based schemes (i.e., schemes based on 1C, 1G) and signal injection based schemes (i.e., schemes based on 1D, 1H) are recommended.
- For high-frequency dc/dc converters, capacitor charging/discharging profiles during transients (i.e., schemes based on 2B, 2D) are recommended for parameters estimation. Although low-cost signal processing circuits are required, high-precision and high-frequency sampling devices are avoided.
- Data training schemes without additional hardware circuits, sensors and external interference are attractive for all types of dc-link applications.

B. Challenges

For CM schemes based on nonelectrical parameters, i.e., industrial instruments measurement based schemes, the main challenge is the lack of uniform end-of-life criteria for capacitors. For CM schemes based on electrical parameter estimation, the challenges are given in the following:

- lack of accurate measurement or estimation of the internal temperature of capacitors, which is essential for parameter calibration;
- additional hardware costs, software costs or external interference for CM;
- measurement noise of voltage and current in harsh electromagnetic interference (EMI) environment, which introduces inaccurate estimation of R_{ESR} or C ;

- 4) a large amount of sampling data or complex processing data are used to improve estimation accuracy;
- 5) inaccurate estimation of capacitor parameters when systems parameters are varied;
- 6) one CM scheme is difficult to extend to other types of dc-link applications

C. Opportunities

The opportunities can be listed as follows:

- 1) further research in wear-out mechanisms of capacitors to obtain accurate degradation model and end-of-life criteria based on nonelectrical parameters;
- 2) designing of accurate CM schemes for real industrial applications (working in harsh EMI environment) without additional hardware cost and reliability risk. Future studies need to improve estimation accuracy while reducing the complexity of sampling data and algorithms;
- 3) monitoring of capacitors' status while monitoring other key components in converters, such as semiconductor switches;
- 4) designing of low-cost and high-accuracy CM schemes that are suitable for all types of dc-link applications;
- 5) research of CM schemes for other types of power electronic applications such as the submodule capacitors in MMC;
- 6) designing of emerging capacitors with built-in monitoring components such as internal thermal sensors and pressure sensors;
- 7) applying the emerging artificial intelligence technology to CM of capacitors.

REFERENCES

- [1] H. Wang, H. Wang, G. Zhu, and F. Blaabjerg, "An overview of capacitive dc-links-topology derivation and scalability analysis," *IEEE Trans. Power Electron.*, vol. 35, no. 2, pp. 1805–1829, Feb. 2020.
- [2] Z. Liao, N. C. Brooks, and R. C. N. Pilawa-Podgurski, "Design constraints for series-stacked energy decoupling buffers in single-phase converters," *IEEE Trans. Power Electron.*, vol. 33, no. 9, pp. 7305–7308, Sep. 2018.
- [3] H. Wang, P. Davari, H. Wang, D. Kumar, F. Zare, and F. Blaabjerg, "Lifetime estimation of dc-link capacitors in adjustable speed drives under grid voltage unbalances," *IEEE Trans. Power Electron.*, vol. 34, no. 5, pp. 4064–4078, May 2019.
- [4] H. Wen, W. Xiao, X. Wen, and P. Armstrong, "Analysis and evaluation of dc-link capacitors for high-power-density electric vehicle drive systems," *IEEE Trans. Veh. Technol.*, vol. 61, no. 7, pp. 2950–2964, Sep. 2012.
- [5] H. S.-H. Chung, H. Wang, F. Blaabjerg, and M. Pecht, *Reliability of Power Electronic Converter Systems*. London, U.K.: IET, 2015.
- [6] K. Ma, H. Wang, and F. Blaabjerg, "New approaches to reliability assessment: Using physics-of-failure for prediction and design in power electronics systems," *IEEE Power Electron. Mag.*, vol. 3, no. 4, pp. 28–41, Dec. 2016.
- [7] D. Zhou, Y. Song, Y. Liu, and F. Blaabjerg, "Mission profile based reliability evaluation of capacitor banks in wind power converters," *IEEE Trans. Power Electron.*, vol. 34, no. 5, pp. 4665–4677, May 2019.
- [8] H. Wang, M. Liserre, and F. Blaabjerg, "Toward reliable power electronics: Challenges, design tools, and opportunities," *IEEE Ind. Electron. Mag.*, vol. 7, no. 2, pp. 17–26, Jun. 2013.
- [9] S. Yang, D. Xiang, A. Bryant, P. Mawby, L. Ran, and P. Tavner, "Condition monitoring for device reliability in power electronic converters: A review," *IEEE Trans. Power Electron.*, vol. 25, no. 11, pp. 2734–2752, Nov. 2010.
- [10] S. Yang, A. Bryant, P. Mawby, D. Xiang, L. Ran, and P. Tavner, "An industry-based survey of reliability in power electronic converters," *IEEE Trans. Ind. Appl.*, vol. 47, no. 3, pp. 1441–1451, May/Jun. 2011.
- [11] A. Amaral and A. Cardoso, "An experimental technique for estimating the aluminum electrolytic capacitor equivalent circuit, at high frequencies," in *Proc. IEEE Int. Conf. Ind. Technol.*, Dec. 2005, pp. 86–91.
- [12] A. Amaral and A. Cardoso, "An ESR meter for high frequencies," in *Proc. Int. Conf. Power Electron. Drives Syst.*, vol. 2, 2005, pp. 1628–1633.
- [13] A. Amaral and A. Cardoso, "An experimental technique for estimating the ESR and reactance intrinsic values of aluminum electrolytic capacitors," in *Proc. IEEE Instrum. Meas. Technol. Conf.*, Apr. 2006, pp. 1820–1825.
- [14] A. Amaral and A. Cardoso, "Using Newton–Raphson method to estimate the condition of aluminum electrolytic capacitors," in *Proc. IEEE Int. Symp. Ind. Electron.*, Jun. 2007, pp. 827–832.
- [15] A. Amaral and A. Cardoso, "An economic offline technique for estimating the equivalent circuit of aluminum electrolytic capacitors," *IEEE Trans. Instrum. Meas.*, vol. 57, no. 12, pp. 2697–2710, Dec. 2008.
- [16] A. Amaral, G. Buatti, H. Ribeiro, and A. Cardoso, "Using DFT to obtain the equivalent circuit of aluminum electrolytic capacitors," in *Proc. 7th Int. Conf. Power Electron. Drive Syst.*, Nov. 2007, pp. 434–438.
- [17] A. Amaral and A. Cardoso, "A simple offline technique for evaluating the condition of aluminum electrolytic capacitors," *IEEE Trans. Ind. Electron.*, vol. 56, no. 8, pp. 3230–3237, Aug. 2009.
- [18] A. Amaral and A. Cardoso, "An automatic technique to obtain the equivalent circuit of aluminum electrolytic capacitors," in *Proc. IEEE 34th Annu. Conf. Ind. Electron.*, Nov. 2008, pp. 539–544.
- [19] A. Amaral and A. Cardoso, "Simple experimental techniques to characterize capacitors in a wide range of frequencies and temperatures," *IEEE Trans. Instrum. Meas.*, vol. 59, no. 5, pp. 1258–1267, May 2010.
- [20] A. M. R. Amaral and A. J. Marques Cardoso, "Using a simple charge-discharge circuit to estimate capacitors equivalent circuit at their operating conditions," in *Proc. IEEE Instrum. Meas. Technol. Conf.*, 2009, pp. 737–742.
- [21] K. M. Tsang and W. L. Chan, "Low-cost sensing of equivalent series resistance for electrolytic capacitors," *IET Power Electron.*, vol. 2, no. 5, pp. 555–562, Sep. 2009.
- [22] K. M. Tsang and W. L. Chan, "Simple method for measuring the equivalent series inductance and resistance of electrolytic capacitors," *IET Power Electron.*, vol. 3, no. 4, pp. 465–471, Jul. 2010.
- [23] A. Amaral and A. Cardoso, "Using a sinusoidal PWM to estimate the ESR of aluminum electrolytic capacitors," in *Proc. Int. Conf. Power Eng., Energy Electr. Drives*, Mar. 2009, pp. 691–696.
- [24] A. M. R. Amaral and A. J. Marques Cardoso, "Estimating aluminum electrolytic capacitors condition using a low frequency transformer together with a DC power supply," in *Proc. IEEE Int. Symp. Ind. Electron.*, 2010, pp. 815–820.
- [25] P. Sundararajan *et al.*, "Condition monitoring of dc-link capacitors using goertzel algorithm for failure precursor parameter and temperature estimation," *IEEE Trans. Power Electron.*, vol. 35, no. 6, pp. 6386–6396, Jun. 2020.
- [26] P. Sundararajan, M. H. M. Sathik, F. Sasongko, C. S. Tan, M. Tariq, and R. Simanjorang, "Online condition monitoring system for dc-link capacitor in industrial power converters," *IEEE Trans. Ind. Appl.*, vol. 54, no. 5, pp. 4775–4785, Sep./Oct. 2018.
- [27] A. Wechsler, B. C. Mecrow, D. J. Atkinson, J. W. Bennett, and M. Benarous, "Condition monitoring of DC-Link capacitors in aerospace drives," *IEEE Trans. Ind. Appl.*, vol. 48, no. 6, pp. 1866–1874, Nov. 2012.
- [28] M. Makdassi, A. Sari, G. Aubard, P. Venet, C. Joubert, and J. Duwattez, "Online health monitoring of metallized polymer film capacitors for avionics applications," in *Proc. IEEE 24th Int. Symp. Ind. Electron.*, Jun. 2015, pp. 1296–1301.
- [29] S. Lee *et al.*, "A new strategy for condition monitoring of adjustable speed induction machine drive systems," *IEEE Trans. Power Electron.*, vol. 26, no. 2, pp. 389–398, Feb. 2011.
- [30] Y. Yu, T. Zhou, M. Zhu, and D. Xu, "Fault diagnosis and life prediction of DC-link aluminum electrolytic capacitors used in three-phase AC/DC/AC converters," in *Proc. 22nd Int. Conf. Instrum., Meas., Comput., Commun. Control*, Harbin, China, 2012, pp. 825–830.
- [31] K.-W. Lee, M. Kim, J. Yoon, S. B. Lee, and J.-Y. Yoo, "Condition monitoring of DC-link electrolytic capacitors in adjustable-speed drives," *IEEE Trans. Ind. Appl.*, vol. 44, no. 5, pp. 1606–1613, Sep./Oct. 2008.
- [32] D. C. Lee, K. J. Lee, J. K. Seok, and J. W. Choi, "Online capacitance estimation of DC-link electrolytic capacitors for three-phase AC/DC/AC PWM converters using recursive least squares method," *IEE Proc.-Elect. Power Appl.*, vol. 152, no. 6, pp. 1503–1508, Nov. 2005.
- [33] X. S. Pu, T. H. Nguyen, D. C. Lee, K. B. Lee, and J. M. Kim, "Fault diagnosis of DC-link capacitors in three-phase AC/DC PWM converters by online estimation of equivalent series resistance," *IEEE Trans. Ind. Electron.*, vol. 60, no. 9, pp. 4118–4127, Sep. 2013.

- [34] A. G. Abo-Khalil and D. C. Lee, "DC-link capacitance estimation in AC/DC/AC PWM converters using voltage injection," *IEEE Trans. Ind. Appl.*, vol. 44, no. 5, pp. 1631–1637, Sep./Oct. 2008.
- [35] X. Pu, T. H. Nguyen, D. C. Lee, and S. G. Lee, "Capacitance estimation of DC-link capacitors for single-phase PWM converters," in *Proc. IEEE 6th Int. Power Electron. Motion Control Conf.*, 2009, pp. 1656–1661.
- [36] T. H. Nguyen and D. C. Lee, "Deterioration monitoring of DC-link capacitors in AC machine drives by current injection," *IEEE Trans. Power Electron.*, vol. 30, no. 3, pp. 1126–1130, Mar. 2015.
- [37] E. Aelioza, J. H. Kim, P. Enjeti, and P. Ruminot, "A real time method to estimate electrolytic capacitor condition in PWM adjustable speed drives and uninterruptible power supplies," in *Proc. IEEE 36th Power Electron. Specialists Conf.*, 2005, pp. 2867–2872.
- [38] M. A. Vogelsberger, T. Wiesinger, and H. Ertl, "Life-cycle monitoring and voltage-managing unit for DC-link electrolytic capacitors in PWM converters," *IEEE Trans. Power Electron.*, vol. 26, no. 2, pp. 493–503, Feb. 2011.
- [39] Y. Wu and X. Du, "A VEN condition monitoring method of DC-link capacitors for power converters," *IEEE Trans. Ind. Electron.*, vol. 66, no. 2, pp. 1296–1306, Feb. 2019.
- [40] M. Kim, S. Sull, and J. Lee, "Condition monitoring of dc-link capacitors in drive system for electric vehicles," in *Proc. IEEE Veh. Power Propulsion Conf.*, Seoul, South Korea, Oct. 9–12, 2012, pp. 633–637.
- [41] H. Li, D. Xiang, X. Han, X. Zhong, and X. Yang, "High-accuracy capacitance monitoring of dc-link capacitor in VSI systems by LC resonance," *IEEE Trans. Power Electron.*, vol. 34, no. 12, pp. 12200–12211, Dec. 2019.
- [42] G. Buiatti, J. Martin-Ramos, A. Amaral, P. Dworakowski, and A. M. Cardoso, "Condition monitoring of metallized polypropylene film capacitors in railway power trains," *IEEE Trans. Instrum. Meas.*, vol. 58, no. 10, pp. 3796–3805, Oct. 2009.
- [43] H. Soliman, I. Abdelsalam, H. Wang, and F. Blaabjerg, "Artificial neural network based dc-link capacitance estimation in a diode-bridge front-end inverter system," in *Proc. IEEE 3rd Int. Future Energy Electron. Conf. ECCE Asia*, 2017, pp. 196–201.
- [44] H. Soliman, H. Wang, B. Gadalla, and F. Blaabjerg, "Condition monitoring for DC-link capacitors based on artificial neural network algorithm," in *Proc. IEEE 5th Int. Conf. Power Eng., Energy Electr. Drives*, May. 2015, pp. 587–591.
- [45] H. Soliman, H. Wang, and F. Blaabjerg, "Capacitance estimation for dc-link capacitors in a back-to-back converter based on artificial neural network algorithm," in *Proc. IEEE 8th Int. Power Electron. Motion Control Conf.*, May 2016, pp. 3682–3688.
- [46] H. Soliman, P. Davari, H. Wang, and F. Blaabjerg, "Capacitance estimation algorithm based on DC-link voltage harmonics using artificial neural network in three-phase motor drive systems," in *Proc. IEEE Energy Convers. Congr. Expo.*, 2017, pp. 5795–5802.
- [47] T. Kamel, Y. Biletskiy, and L. Chang, "Capacitor aging detection for the dc filters in the power electronic converters using ANFIS algorithm," in *Proc. 28th Can. Conf. Elect. Comput. Eng.*, May 2015, pp. 663–668.
- [48] M. W. Ahmad, P. N. Kumar, A. Arya, and S. Anand, "Noninvasive technique for dc-link capacitance estimation in single-phase inverters," *IEEE Trans. Power Electron.*, vol. 33, no. 5, pp. 3693–3696, May 2018.
- [49] A. Arya, M. W. Ahmad, N. Agarwal, and S. Anand, "Capacitor impedance estimation utilizing dc-link voltage oscillations in single phase inverter," *IET Power Electron.*, vol. 10, no. 9, pp. 1046–1053, 2017.
- [50] N. Agarwal, M. W. Ahmad, and S. Anand, "Condition monitoring of dc-link capacitor utilizing zero state of solar PV H5 inverter," in *Proc. 10th Int. Conf. Comput., Power Electron. Power Eng.*, 2016, pp. 174–179.
- [51] N. Agarwal, M. W. Ahmad, and S. Anand, "Quasi-online technique for health monitoring of capacitor in single-phase solar inverter," *IEEE Trans. Power Electron.*, vol. 33, no. 6, pp. 5283–5291, Jun. 2018.
- [52] Y. Gupta, M. W. Ahmad, S. Narale, and S. Anand, "Health estimation of individual capacitors in a bank with reduced sensor requirements," *IEEE Trans. Ind. Electron.*, vol. 66, no. 9, pp. 7250–7259, Sep. 2019.
- [53] P. Sun, C. Gong, X. Du, Q. Luo, H. Wang, and L. Zhou, "Online condition monitoring for both IGBT module and DC-link capacitor of power converter based on short-circuit current simultaneously," *IEEE Trans. Ind. Electron.*, vol. 64, no. 5, pp. 3662–3671, May 2017.
- [54] A. Arya, M. W. Ahmad, and S. Anand, "Online monitoring of power extraction efficiency for minimizing payback period of solar PV system," in *Proc. IEEE Int. Conf. Ind. Technol.*, Seville, Spain, Mar. 2015, pp. 2863–2868.
- [55] N. Agarwal, A. Arya, M. W. Ahmad, and S. Anand, "Lifetime monitoring of electrolytic capacitor to maximize earnings from grid-feeding PV system," *IEEE Trans. Ind. Electron.*, vol. 63, no. 11, pp. 7049–7058, Nov. 2016.
- [56] K. Laadjal, M. Sahraoui, A. J. M. Cardoso, and A. M. R. Amaral, "Online estimation of aluminum electrolytic-capacitors parameters using a modified Prony's method," *IEEE Trans. Ind. Appl.*, vol. 54, no. 5, pp. 4764–4774, Sep./Oct. 2018.
- [57] A. M. R. Amaral and A. J. M. Cardoso, "State condition estimation of aluminum electrolytic capacitors used on the primary side of ATX power supplies," in *Proc. IEEE Ind. Electron. Conf.*, Nov. 2009, pp. 442–447.
- [58] A. M. Imam, D. M. Divan, R. G. Harley, and T. G. Habtler, "Real-time condition monitoring of the electrolytic capacitors for power electronics applications," in *Proc. IEEE Appl. Power Electron. Conf.*, Mar. 2007, pp. 1057–1061.
- [59] K. Abdennadher, P. Venet, G. Rojat, J. M. Retif, and C. Rosset, "A real-time predictive-maintenance system of aluminum electrolytic capacitors used in uninterrupted power supplies," *IEEE Trans. Ind. Appl.*, vol. 46, no. 4, pp. 1644–1652, Jul./Aug., 2010.
- [60] W. G. Lu, X. Lu, J. Han, Z. Zhao, and X. Du, "Online estimation of ESR for dc-link capacitor of boost pfc converter using wavelet transform based time-frequency analysis method," *IEEE Trans. Power Electron.*, vol. 35, no. 8, pp. 7755–7764, Aug. 2020.
- [61] K. Yao, W. Tang, X. Bi, and J. Lyu, "An online monitoring scheme of DC-link capacitor's ESR and C for a boost PFC converter," *IEEE Trans. Power Electron.*, vol. 31, no. 8, pp. 5944–5951, Aug. 2016.
- [62] Y. M. Chen, H. C. Wu, M. W. Chou, and K. Y. Lee, "Online failure prediction of the electrolytic capacitor for LC filter of switching-mode power converters," *IEEE Trans. Ind. Electron.*, vol. 55, no. 1, pp. 400–406, Jan. 2011.
- [63] A. Imam, T. Habtler, R. Harley, and D. Divan, "LMS based condition monitoring of electrolytic capacitor," in *Proc. 31st Annu. Conf. IEEE Ind. Electron. Soc.*, Nov. 2005, pp. 848–853.
- [64] P. Venet, F. Perisse, M. H. El-Husseini, and G. Rojat, "Realization of a smart electrolytic capacitor circuit," *IEEE Ind. Appl. Mag.*, vol. 8, no. 1, pp. 16–20, Jan. 2002.
- [65] A. Lahyani, P. Venet, G. Grellet, and P. Viverge, "Failure prediction of electrolytic capacitors during operating of a switch mode power supply," *IEEE Trans. Power Electron.*, vol. 13, no. 6, pp. 1199–1207, Nov. 1998.
- [66] A. M. R. Amaral and A. J. M. Cardoso, "Use of ESR to predict failure of output filtering capacitors in boost converters," in *Proc. IEEE Int. Symp. Ind. Electron.*, May 2004, pp. 1309–1314.
- [67] H. Givi, E. Farjah, and T. Ghanbari, "Switch fault diagnosis and capacitor lifetime monitoring technique for DC–DC converters using a single sensor," *IET Sci., Meas. Technol.*, vol. 10, no. 5, pp. 513–527, Aug. 2016.
- [68] W. Miao, K. H. Lam, and P. W. T. Pong, "Online monitoring of aluminum electrolytic capacitors in photovoltaic systems by magnetoresistive sensors," *IEEE Sensors J.*, vol. 20, no. 2, pp. 767–777, Jan. 2020.
- [69] W. Miao, X. Liu, K. H. Lam, and P. W. T. Pong, "Condition monitoring of electrolytic capacitors in boost converters by magnetic sensors," *IEEE Sens. J.*, vol. 19, no. 22, pp. 10393–10402, Nov. 2019.
- [70] G. H. Wang, Y. Guan, J. Zhang, L. F. Wu, and X. Y. Zheng, "ESR estimation method for DC–DC converters based on improved EMD algorithm," in *Proc. IEEE Conf. Prognostics Syst. Health Manage.*, May. 2012, pp. 1–6.
- [71] L. Ren and C. Gong, "Online estimation scheme of output capacitor's ESR and $\tan\delta$ for Buck converter," *IET Power Electron.*, vol. 12, no. 11, pp. 2978–2986, 2019.
- [72] E. Farjah, H. Givi, and T. Ghanbari, "Application of an efficient Rogowski coil sensor for switch fault diagnosis and capacitor ESR monitoring in nonisolated single switch DC–DC converters," *IEEE Trans. Power Electron.*, vol. 32, no. 2, pp. 1442–1456, Feb. 2017.
- [73] H. Givi, E. Farjah, and T. Ghanbari, "A comprehensive monitoring system for online fault diagnosis and aging detection of non-isolated dc–dc converters' components," *IEEE Trans. Power Electron.*, vol. 34, no. 7, pp. 6858–6875, Jul. 2019.
- [74] A. M. R. Amaral and A. J. M. Cardoso, "On-line fault detection of aluminum electrolytic capacitors, in step-down dc–dc converters, using input current and output voltage ripple," *IET Power Electron.*, vol. 5, no. 3, pp. 315–322, 2012.
- [75] A. Amaral and A. Cardoso, "A non-invasive technique for fault diagnosis of SMPS," in *Proc. Power Electron. Spec. Conf.*, Jun. 2008, pp. 2097–2102.

- [76] K. Yao, W. Tang, W. Hu, and J. Lyu, "A current-sensorless online ESR and C identification method for output capacitor of buck converter," *IEEE Trans. Power Electron.*, vol. 30, no. 12, pp. 6993–7005, Dec. 2015.
- [77] J. Gao, D. Huang, and J. Lu, "Online output capacitor monitor for buck dc–dc converter," in *Proc. Prognostics Syst. Health Manage. Conf. (PHM-Chongqing)*, 2018, pp. 802–806.
- [78] A. Amaral and A. Cardoso, "Using input current and output voltage ripple to estimate the output filter condition of switch mode dc/dc converters," in *Proc. IEEE Int. Symp. Diagnostics Elect. Mach., Power Electron. Drives*, Aug. 2009, pp. 1–6.
- [79] G. M. Buiatti, J. A. Martin-Ramos, C. H. R. Garcia, and A. M. R. Amaral, "An online and noninvasive technique for the condition monitoring of capacitors in boost converters," *IEEE Trans. Instrum. Meas.*, vol. 59, no. 8, pp. 2134–2143, Aug. 2011.
- [80] L. Ren, C. Gong, and Y. Zhao, "An online ESR estimation method for output capacitor of boost converter," *IEEE Trans. Power Electron.*, vol. 34, no. 10, pp. 10153–10165, Oct. 2019.
- [81] M. Ahmad, A. Arya, and S. Anand, "An online technique for condition monitoring of capacitor in PV system," in *Proc. IEEE Int. Conf. Ind. Technol.*, Mar. 2015, pp. 920–925.
- [82] M. W. Ahmad, N. Agarwal, and S. Anand, "Online monitoring technique for aluminum electrolytic capacitor in solar PV-based DC system," *IEEE Trans. Ind. Electron.*, vol. 63, no. 11, pp. 7059–7066, Nov. 2016.
- [83] K. Yao, C. Cao, and S. Yang, "Noninvasive online condition monitoring of output capacitor's ESR and C for a flyback converter," *IEEE Trans. Instrum. Meas.*, vol. 66, no. 12, pp. 3190–3199, Dec. 2017.
- [84] K. Yao *et al.*, "A noninvasive online monitoring method of output capacitor's C and ESR for DCM flyback converter," *IEEE Trans. Power Electron.*, vol. 34, no. 6, pp. 5748–5763, Jun. 2019.
- [85] H. Ma, X. Mao, N. Zhang, and D. Xu, "Parameter identification of power electronic circuits based on hybrid model," in *Proc. IEEE Power Electron. Spec. Conf.*, Jun. 12–16, 2005, pp. 2855–2860.
- [86] H. Ma and L. G. Wang, "Fault diagnosis and failure prediction of aluminum electrolytic capacitor in power electronic converters," in *Proc. IEEE Ind. Electron. Conf.*, 2005, pp. 842–847.
- [87] G. M. Buiatti, A. M. R. Amaral, and A. J. Marques Cardoso, "An unified method for estimating the parameters of non-isolated DC/DC converters using continuous time models," in *Proc. 29th Int. Telecommun. Energy Conf.*, 2007, pp. 334–341.
- [88] G. Buiatti and A. Amaral, "Parameter estimation of a dc/dc buck converter using a continuous time model," in *Proc. Eur. Conf. Power Electron. Appl.*, 2007, pp. 1–8.
- [89] Z. Cen and P. Stewart, "Condition parameter estimation for photovoltaic buck converters based on adaptive model observers," *IEEE Trans. Rel.*, vol. 66, no. 1, pp. 148–160, Mar. 2017.
- [90] G. M. Buiatti, A. M. Amaral, and A. J. M. Cardoso, "ESR estimation method for dc/dc converters through simplified regression models," in *Proc. Conf. Rec. IEEE 42nd Ind. Appl. Conf.*, Sep. 2007, pp. 2289–2294.
- [91] G. M. Buiatti, A. M. Amaral, and A. J. M. Cardoso, "An online technique for estimating the parameters of passive components in nonisolated DC/DC converters," in *Proc. IEEE Int. Symp. Ind. Electron.*, 2007, pp. 606–610.
- [92] L. Ren and C. Gong, "Modified hybrid model of boost converters for parameter identification of passive components," *IET Power Electron.*, vol. 11, no. 4, pp. 764–771, 2018.
- [93] Y. Peng and H. Wang, "Parameters identification of buck converter based on dynamic characteristics," in *Proc. IEEE Int. Power Electron. Conf.*, 2019, pp. 3071–3076.
- [94] Y. Peng and H. Wang, "Application of digital twin concept in condition monitoring for dc–dc converter," in *Proc. IEEE Energy Convers. Congr. Expo.*, Baltimore, MD, USA, 2019, pp. 2199–2204.
- [95] M. W. Ahmad, N. Agarwal, P. N. Kumar, and S. Anand, "Low-frequency impedance monitoring and corresponding failure criteria for aluminum electrolytic capacitors," *IEEE Trans. Ind. Electron.*, vol. 64, no. 7, pp. 5657–5666, Jul. 2017.
- [96] M. Algreer, M. Armstrong, and D. Giaouris, "Active online system identification of switch mode DC–DC power converter based on efficient recursive DCD-IIR adaptive filter," *IEEE Trans. Power Electron.*, vol. 27, no. 11, pp. 4425–4435, Nov. 2012.
- [97] M. Ahmeid, M. Armstrong, S. Gadoue, M. Algreer, and P. Missailidis, "Real-time parameter estimation of DC–DC converters using a self-tuned Kalman filter," *IEEE Trans. Power Electron.*, vol. 32, no. 7, pp. 5666–5674, Jul. 2017.
- [98] B. X. Li and K. S. Low, "Low sampling rate online parameters monitoring of DC–DC converters for predictive maintenance using biogeography-based optimization," *IEEE Trans. Power Electron.*, vol. 31, no. 4, pp. 2870–2879, Apr. 2016.
- [99] Z. Zhao, W. G. Lu, P. Davari, X. Du, H. H. Iu, and F. Blaabjerg, "An online parameters monitoring method for output capacitor of buck converter based on large-signal load transient trajectory analysis," *IEEE J. Emerg. Sel. Topics Power Electron.*, to be published, doi: 10.1109/JESTPE.2020.2964068.
- [100] H. Nakao, Y. Yonezawa, T. Sugawara, Y. Nakashima, and F. Kurokawa, "Online evaluation method of electrolytic capacitor degradation for digitally controlled SMPS failure prediction," *IEEE Trans. Power Electron.*, vol. 33, no. 3, pp. 2552–2558, Mar. 2018.
- [101] J. Hannonen, J. Honkanen, J. P. Strom, T. Karkkainen, S. Raisanen, and P. Silventoinen, "Capacitor aging detection in a dc–dc converter output stage," *IEEE Trans. Ind. Appl.*, vol. 52, no. 4, pp. 3224–3233, Jul./Aug. 2016.
- [102] H. Wang and F. Blaabjerg, "Reliability of capacitors for dc-link applications in power electronic converters—an overview," *IEEE Trans. Ind. Appl.*, vol. 50, no. 5, pp. 3569–3578, Sep. 2014.
- [103] H. Soliman, H. Wang, and F. Blaabjerg, "A review of the condition monitoring of capacitors in power electronic converters," *IEEE Trans. Ind. Appl.*, vol. 52, no. 6, pp. 4976–4989, Nov./Dec. 2016.
- [104] Type SLXP 85°C Snap-In Aluminum Electrolytic, CDE Cornell Dubilier, New Bedford, MA, USA, Mar. 19, 2020. [Online]. Available: <http://www.cde.com/resources/catalogs/SLXP.pdf>, Accessed: Sep. 2020.
- [105] Film Capacitors—Metallized Polypropylene Film Capacitors, TDK Corporation, Tokyo, Japan, Jun. 7, 2018. [Online]. Available: https://www.tdk-electronics.tdk.com/inf/20/20/db/fc_2009/MKP_B32774_778.pdf, Accessed: Sep. 2020.
- [106] Metal Terminal Type Multilayer Ceramic Capacitors for Automotive –KCM55WC71E107MH13, Murata Manufacturing Co., Ltd., Nagaokakyo, Kyoto, Japan, Apr. 8, 2020. [Online]. Available: https://ds.murata.co.jp/simserve/characteristics?ReqType=TechPDF&partnumber=KCM55WC71E107MH13&lang=en&techpdfname=technical_pdf_Capacitor01, Accessed: Sep. 2020.
- [107] A. Gupta, O. P. Yadav, D. DeVoto, and J. Major, "A review of degradation behavior and modeling of capacitors," in *Proc. Int. Tech. Conf. Exhib. Packag. Integr. Electron. Photon. Microsyst.*, Oct. 2018, pp. 1–10.
- [108] S. Gulbrandsen, J. Arnold, N. Kirsch, and G. Caswell, "A new method for testing electrolytic capacitors to compare life expectancy," in *Proc. Additional Conf. (Device Packag., HiTEC, HiTEN, CICMT)*, Jan. 2014, pp. 1759–1786.
- [109] A. Shrivastava, M. H. Azarian, C. Morillo, B. Sood, and M. Pecht, "Detection and reliability risks of counterfeit electrolytic capacitors," *IEEE Trans. Rel.*, vol. 63, no. 2, pp. 468–479, Jun. 2014.
- [110] C. Andersson, J. Ingman, E. Värescon, and M. Kiviniemi, "Detection of cracks in multilayer ceramic capacitors by X-ray imaging," *Microelectron. Rel.*, vol. 64, pp. 352–356, 2016.
- [111] L. Bechou, S. Mejdi, Y. Ousten, and Y. Danto, "Non-destructive detection and localization of defects in multilayer ceramic chip capacitors using electromechanical resonances," *Qual. Rel. Eng. Int.*, vol. 12, pp. 43–53, 1996.
- [112] S. Levikari, T. J. Kärkkäinen, C. Andersson, J. Tamminen, and P. Silventoinen, "Acoustic detection of cracks and delamination in multilayer ceramic capacitors," *IEEE Trans. Ind. Appl.*, vol. 55, no. 2, pp. 1787–1794, Mar./Apr. 2019.
- [113] C. Andersson, O. Kristensen, S. Miller, T. Gloor, and F. Iannuzzo, "Lock-in thermography failure detection on multilayer ceramic capacitors after flex cracking and temperature–humidity–bias stress," *IEEE J. Emerg. Sel. Top. Power Electron.*, vol. 6, no. 4, pp. 2254–2261, Dec. 2018.
- [114] H. Wang, R. Zhu, H. Wang, M. Liserre, and F. Blaabjerg, "A thermal modeling method considering ambient temperature dynamics," *IEEE Trans. Power Electron.*, vol. 35, no. 1, pp. 6–9, Jan. 2020.
- [115] Z. Dou, X. Rong, B. Alfonso, Q. Javaid, and P. Cynthia, *Performance of Aluminum Electrolytic Capacitors and Influence of Aluminum Cathode Foils*, CARTS Europe, 2010.
- [116] B. Sun, X. J. Fan, C. Qian, and G. Q. Zhang, "PoF-simulation-assisted reliability prediction for electrolytic capacitor in LED drivers," *IEEE Trans. Ind. Electron.*, vol. 63, no. 11, pp. 6726–6735, Nov. 2016.
- [117] Y. Zhou, X. Ye, and G. Zhai, "Degradation model and maintenance strategy of the electrolytic capacitors for electronics applications," in *Proc. Prognostics Syst. Health Manage. Conf.*, pp. 1–6, May 2011.
- [118] M. Makdassi, A. Sari, and P. Venet, "Metallized polymer film capacitors ageing law based on capacitance degradation," *Microelectron. Rel.*, vol. 54, pp. 1823–1827, 2014.

- [119] D. N. Donahoe, "Moisture in multilayer ceramic capacitors," PhD dissertation, Dept. Mechanical Eng., Univ. Maryland, College Park, MD, USA, 2005.
- [120] F. Perisse, P. Venet, G. Rojat, and J. M. Retif, "Simple model of electrolytic capacitor taking into account the temperature and aging time," *Arch. Elektrotech.*, vol. 88, no. 2, pp. 89–95, Jan. 2006.
- [121] Nichicon, Corp., Kyoto, Japan. "General description of aluminum electrolytic capacitors," Sep. 22, 2011. [Online]. Available: <http://www.nichicon.co.jp/english/products/pdf/aluminum.pdf>, Accessed: Sep. 2020.
- [122] "Film capacitors-general technical information," TDK Corporation, Tokyo, Japan, Jun. 7, 2018. [Online]. Available: <https://www.tdk-electronics.tdk.com/download/530754/480aeb04c789e45ef5bb9681513474ba/pdf-generaltechnicalinformation.pdf>, Accessed: Sep. 2020.
- [123] "The temperature characteristics of electrostatic capacitance," Oct. 15, 2012. [Online]. Available: <https://article.murata.com/en-global/article/temperature-characteristics-electrostatic-capacitance>, Accessed: Sep. 2020.
- [124] "Multilayer ceramic capacitors-performance characteristics," CDE Cornell Dubilier, Massachusetts, USA, Jan. 10, 2007. [Online]. Available: <https://www.cde.com/resources/catalogs/ceramperf.pdf>, Accessed: Sep. 2020.
- [125] Z. Zhao, W. G. Lu, W. Chen, X. Du, and H. H. Iu, "Multi-period frame transient switching control for low-voltage high-current buck converter with a controlled coupled inductor," *IEEE Trans. Power Electron.*, vol. 34, no. 10, pp. 9743–9757, Oct. 2019.
- [126] A. Braham, A. Lahyani, P. Venet, and N. Rejeb, "Recent developments in fault detection and power loss estimation of electrolytic capacitors," *IEEE Trans. Power Electron.*, vol. 25, no. 1, pp. 33–43, Jan. 2010.
- [127] Z. Wang, Y. Zhang, H. Wang, and F. Blaabjerg, "Capacitor condition monitoring based on the dc-side start-up of modular multilevel converters," *IEEE Trans. Power Electron.*, vol. 35, no. 6, pp. 5589–5593, Jun. 2020.



Zhaoyang Zhao (Student Member, IEEE) received the B.S. and M.S. degrees in electrical engineering from Northeast Agricultural University, Harbin, China, in 2014 and 2017, respectively. He is currently working toward the Ph.D. degree in electrical engineering with the School of Electrical Engineering, Chongqing University, Chongqing, China.

From 2019 to 2020, he was a Visiting Ph.D. Student with the Department of Energy Technology, Aalborg University, Aalborg, Denmark. His research interests include condition monitoring, reliability assessment, and control of power electronic converters.



Pooya Davari (Senior Member, IEEE) received the B.Sc. and M.Sc. degrees in electronic engineering from the University of Mazandaran Noushirvani, Iran, in 2004 and 2008, respectively, and the Ph.D. degree in power electronics from the Queensland University of Technology (QUT), Brisbane, Australia, in 2013.

From 2005 to 2010, he was involved in several electronics and power electronics projects, as a Development Engineer. From 2013 to 2014, he was with QUT, as a Lecturer. In 2014, he joined as a Postdoc with Aalborg University, where he is currently an Associate Professor. He has been focusing on EMI, power quality and harmonic mitigation analysis and control in power electronic systems. He has published more than 140 technical papers.

Dr. Davari served as a Guest Associate Editor of *IET Journal of Power Electronics*, *IEEE ACCESS JOURNAL*, *Journal of Electronics*, and *Journal of Applied Sciences*. He is an Associate Editor of *Journal of Power Electronics*, Associate Editor of *IET Electronics*, Editorial Board Member of *EPE Journal*, and *Journal of Applied Sciences*. He is member of the International Scientific Committee (ISC) of EPE (ECCE Europe) and a member of Joint Working Group 6 and Working Group 8 at the IEC standardization TC77A. He is the recipient of a research grant from the Danish Council of Independent Research (DFF-FTP) in 2016, and the 2020 IEEE EMC Society Young Professional Award for his contribution to EMI and harmonic mitigation and modeling in power electronic applications. He is currently Editor-in-Chief of Circuit World Journal.



Weiguo Lu (Member, IEEE) received the B.S., M.S., and Ph.D. degrees in electrical engineering from Chongqing University, Chongqing, China, in 2000, 2003, and 2008, respectively.

He is currently a Professor with the School of Electrical Engineering, Chongqing University, Chongqing. He is the author or co-author of more than 20 papers in journal or conference proceedings. His current research interests include the stability analysis and control strategies of switching power converters, and magnetic-resonance wireless power transfer.



Huai Wang (Senior Member, IEEE) received the B.E. degree in electrical engineering from the Huazhong University of Science and Technology, Wuhan, China, in 2007 and, the Ph.D. degree in power electronics from the City University of Hong Kong, Hong Kong, in 2012.

He is currently a Professor with the Center of Reliable Power Electronics, Department of Energy Technology, Aalborg University, Denmark. He was a Visiting Scientist with the ETH Zurich, Switzerland, from August to September 2014, and with the Massachusetts Institute of Technology, MA, USA, from September to November 2013. He was with the ABB Corporate Research Center, Switzerland, in 2009. His research addresses the fundamental challenges in modeling and validation of power electronic component failure mechanisms, and application issues in system-level predictability, condition monitoring, circuit architecture, and robustness design.

Dr. Wang received the Richard M. Bass Outstanding Young Power Electronics Engineer Award from the IEEE Power Electronics Society in 2016, and the Green Talents Award from the German Federal Ministry of Education and Research in 2014. He is currently the Chair of IEEE PELS/IAS/IES Chapter in Denmark. He serves as an Associate Editor of *IET Electronics Letters*, *IEEE JOURNAL OF EMERGING AND SELECTED TOPICS IN POWER ELECTRONICS*, and *IEEE TRANSACTIONS ON POWER ELECTRONICS*.



Frede Blaabjerg (Fellow, IEEE) received the Ph.D. degree in electrical engineering from Aalborg University, Aalborg, Denmark, in 1995.

He was with ABB-Scandia, Randers, Denmark, from 1987 to 1988. He became an Assistant Professor in 1992, an Associate Professor in 1996, and a Full Professor of power electronics and drives in 1998. In 2017, he became a Villum Investigator. He is honoris causa with University Politehnica Timisoara, Romania, and Tallinn Technical University, Estonia. His current research interests include power electronics and its applications such as in wind turbines, PV systems, reliability, harmonics, and adjustable speed drives. He has published more than 600 journal papers in the fields of power electronics and its applications. He is the co-author of four monographs, and editor of ten books in power electronics and its applications.

Dr. Blaabjerg has received 30 IEEE Prize Paper Awards, the IEEE PELS Distinguished Service Award in 2009, the EPE-PEMC Council Award in 2010, the IEEE William E. Newell Power Electronics Award 2014, and the Villum Kann Rasmussen Research Award 2014. He was the Editor-in-Chief of the *IEEE TRANSACTIONS ON POWER ELECTRONICS* from 2006 to 2012. He has been a Distinguished Lecturer for the IEEE Power Electronics Society from 2005 to 2007 and for the IEEE Industry Applications Society from 2010 to 2011 as well as from 2017 to 2018. In 2019–2020, he was the President of IEEE Power Electronics Society. He is the Vice-President of the Danish Academy of Technical Sciences too. He was nominated in 2014–2018 by Thomson Reuters to be between the 250 most-cited researchers in engineering in the world.